Bogdan-Marian P. VERDETE

DOCTORAL THESIS

PhD. supervisor
Prof. Phd. Cristina PUPĂZĂ

- 2023-

Bogdan-Marian P. VERDETE

DOCTORAL THESIS

The influence of the welding parameters on the heat transfer that occurs during the robotic surfacing weld processes

SUMMARY

PhD. supervisor
Prof. PhD. Cristina PUPĂZĂ

- 2023 -

University POLITEHNICA of Bucharest

CSUD Decision UPB no. 1051 from 10.07.2023

Bogdan-Marian P. VERDETE

DOCTORAL THESIS

Influenţa parametrilor regimului de sudare asupra transferului de căldură la depunerea de material prin sudare robotizată

The influence of the welding parameters on the heat transfer that occurs during the robotic surfacing weld processes

DOCTORAL COMMITTEE

Committee Chairperson	Prof.univ.dr.ing. Miron ZAPCIU	University POLITEHNICA of Bucharest
PhD. Supervisor	Prof.univ.dr.ing. Cristina PUPĂZĂ	
Member	Prof.univ.dr.ing. Sever-Gabriel RACZ	"Lucian Blaga" University of Sibiu
Member	Prof.univ.dr.ing. Ionel STAREȚU	Transilvania University of Brașov
Member	Prof.univ.dr.ing. Cătălin Gheorghe AMZA	University POLITEHNICA of Bucharest

- 2023 -

Outline

The research context

Robot welding is essential in the current industry due to the benefits. By integrating industrial robots into welding processes, increased efficiency and productivity are attained. This is due to the superior speed and work accuracy. The quality of the finished products becomes consistent, as the errors caused by human operators are eliminated. Safety in operation is also ensured, by reducing the risks associated with welding technologies. Robotic welding contributes to long-term cost reduction by minimizing material losses. It offers flexibility and adaptability, as it can be programmed for different types of parts and technologies. By reducing the dependency on the human decision factor, robotic welding ensures stability and continuity in production processes, regardless of market fluctuations.

The deposition of material by robotic welding is important in industry because it enables the rapid repair of worn or damaged parts or components, thus extending their life and avoiding the high costs associated with complete replacement.

The thermal analysis of the robotic welding material deposition processes is crucial in the current industrial context. It allows the evaluation and optimization of the heat transfer parameters, such as temperature, heating and cooling speed, as well as the phase changes that occur during welding. By understanding and adequately controlling these parameters, an efficient and high-quality refurbishment of the parts can be ensured. Thermal analysis helps to prevent excessive dilation, cracks and internal stresses, thus ensuring the integrity and optimal performance of the refurbished parts.

Although the literature on this research topic is abundant, a number of questions remain unanswered.

This Doctoral Thesis addresses the numerical and experimental aspects of heat transfer in robotic material deposition technologies.

In the first phase, a steel semi-finished product is used which is subjected to the robotic deposition process of the filler material. A robotic cell devoted to electric arc welding operations under a protective gas environment is used for this purpose. Experimental techniques necessary to acquire temperatures at the level of the weld pool and the base material are highlighted.

A simulation model based on computational fluid dynamics and the finite element method is developed. The purpose of this is to reproduce heat transfer by convection and conduction that occurs due to the welding process.

The validation of the simulation approach is done by considering different values of the gas flow rate. It is experimentally observed that the results of the thermal analysis only partially match the physically measured ones.

In this sense, a correlation was identified between the welding regime parameters and the conductivity and capacitance of the model that occurs at the interaction between the base material and the filler material.

In the last phase, the verification of the macroscopic and microscopic characteristics of the welded samples was carried out. Linearity trends were observed between the conductivity and capacitance corrections and certain parameters evaluated by non-destructive testing. As a result, a multiple linear regression model was developed to increase the degree of generalization of the approach.

Lista of abreviations

No.	Abrev.	Semnificație/ Significance
1	CAD	Proiectare Asistată de Calculator / Computer Aided Design
2	CFD	Dinamica Fluidelor Computațională / Computational Fluid Dynamics
3	CM	Crater marginal / Marginal crater
4	CPS	Sisteme Cyber-Fizice / Cyber Physical Systems
5	CSV	Fișier delimitat cu virgule / Comma Separated Value
6	CZ	Cruste de zgură / Slag crust
7	FOPDT	Sistem de ordin 1 cu întârziere / First order plus dead time system
8	MAG	Metal activ gaz / Metal active gas
9	MEF	Metoda Elementelor Finite / Finite Element Method
10	MIG	Metal inert gaz / Metal inert gas
11	NG	Neuniformități geometrice / Geometric non-uniformities
12	NS	Număr de stropi / Number of droplets
13	PC	Calculator personal / Personal Computer
14	RANS	Reynolds-averaged Navier-Stokes / Reynolds-averaged Navier-Stokes
15	RMS	Eroarea medie pătratică / Mean squared error
16	UE	Uniunea Europeană / The European Union
17	ZIT	Zona influențată termic / Thermal influenced zone

List of symbols

Nr. crt.	Abrev.	Semnificație/ Significance
1	A	Arie / Area
2	A_d	Rata depunerii / Deposition rate
3	B	Lățime cordon sudură / Welded joint width
4	$C(s)$	Mărime de ieșire / Output variable
5	C_{th}	Capacitanța termică / Thermal capacitance
6	C_μ	Constantă / Constant
7	d_g	Debitul de gaz / Gas flow rate
8	$E_{i,j}$	Parametrul vitezei de deformare / Strain rate parameter
9	E_l	Energia liniară / Liniar energy
10	G_k	Energia cinetică turbulentă datorită gradienților medii de viteză / Kinetic energy due to the average velocity gradients
11	h	Înălțime cordon sudură / Welded joint height

12	I	Intensitatea curentului de sudare / Welding current
13	K	Factor de aplificare / Gain
14	l_{cl}	Lungimea liberă a sârmei electrod / Electrode stick-out
15	L_l	Distanța dintre duza de gaz și materialul de sudat / Standoff distance
16	Nu	Numărul lui Nusselt / Nusselt Number
17	P_e	Forța electromagnetică / Electromagnetic force
18	P_p	Forța de propulsie / Propulsion force
19	Pr	Numărul lui Prandtl / Prandtl number
20	q	Căldura transferată între nodurile elementului / Heat between the element nodes
21	R(s)	Mărime de intrare / Input variable
22	Re	Numărul lui Reynolds / Reynolds number
23	R_{th}	Conductanța termică / Thermal conductance
24	S_ε	Termeni definiți de utilizator / User defined terms
25	t_f	Temperatura mediului ambiant / Ambient temperature
26	$T_{i,j}$	Temperaturi nodale / Nodal temperatures
27	t_s	Temperatura suprafeței / Surface temperature
28	U	Tensiunea arcului / Arc voltage
29	v_a	Viteza de avans a sârmei electrod / Wire feed rate
30	v_g	Viteza de curgere a gazului de protecție / Welding gas flow rate
31	v_s	Viteza de sudare / Welding speed
32	Y_M	Contribuția dilatării fluctuante a turbulențelor la viteza de disipare / The contribution of the fluctuating dilation on the turbulent dissipation velocity
33	θ	Întârzierea sistemului / System dead time
34	σ_k	Numărul Prandtl pentru energia cinetică turbulentă / Prandtl number for the kinetic turbulent energy
35	σ_ε	Numărul Prandtl pentru viteza de disipare a turbulențelor / Prandtl number for the turbulence dissipation velocity
36	τ	Constanta de timp a sistemului / Time constant

Chapter 1. Technological considerations

1.1. Technological considerations

Robot welding represents an automated welding process in which an industrial robot carries out the deposition of material/surfacing weld in place of a human operator. From this perspective, the robot is used to generate trajectories in a repetitive manner, being equipped with specific welding equipment. The system can be programmed to perform welds in various positions and angles. In this regard, the process is characterized by a high repeatability. Robot welding is commonly used for the manufacturing of products with a high degree of precision and efficiency, by minimizing human errors and reducing the cycle time [1].

Robot welding is distinguished from other conventional processes by several distinctive features. Controlled by a process controller, robot welding is very accurate, having the ability to generate exact and repeatable trajectories. In addition, an industrial robot can operate without interruption, without the breaks required in manual welding, which makes the welding process more efficient. Therefore, the welded joints achieved by means of robot welding have a superior quality. In addition, the robot can be programmed to carry out a wide range of movements and to perform complex depositions of material/surfacing weld, making this process ideal for mass production [2].

However, there are also disadvantages of robot welding. It can be costly in the implementation phase and can require significant investments in equipment and specialized staff training. Also, adapting to production changes can be difficult. As a rule, each robot welding solution is characteristic of a certain category of welded parts (small, medium, large).

Common robot welding technologies include: electric arc welding, laser welding, plasma welding and electron beam welding. Electric arc welding is the most widely employed technology. It can be of MIG/MAG type (with consumable electrode, in an inert or active gas protection environment). Laser welding uses a laser beam to melt the material and to perform the depositions of material/surfacing weld. Plasma welding involves the use of an ionized gas to produce the heat necessary to melt the material. Electron beam welding requires the operation of the entire technological system in a vacuum. Gas protection welding uses an inert gas to prevent oxidation of the material and to protect the weld. Each technology has its advantages and disadvantages, and the choice of the right technology depends on the application and the material that is welded. Of all the above mentioned welding processes, the most widely used today are those in the category of electric arc welding technologies. All these robot welding processes use electric arc and weld pool protection gas.

The benefits of robot welding include the ability to perform depositions of material/surfacing weld in hazardous or difficult-to-access areas for human operators, thus reducing the risk of accidents. Robot welding can also be more economical than manual welding in the case of a large volume of production and can reduce costs by eliminating defects or scrap parts [3]. Regardless the technological method and procedure, the problem of the final product quality and its optimization is at the center of attention [4]. Therefore, over the years, research has been carried out from which mathematical models have emerged to explain the different phenomena that take place within the process, simulation models have been developed to facilitate research, and more recently for better control, there is a tendency to associate the process with what we call Artificial Intelligence [5].

Chapter 2. Recent trends in robotic welding

2.1 Conclusions regarding the present industrial context of robotic material deposition welding

The study of the recent bibliography highlighted the timeliness and opportunity of the topic addressed in the Doctoral Thesis from the perspective of the refurbishment of parts by electric arc additive manufacturing. The most important parameters, the employed equipment, the need for a systemic approach to the complex phenomena that occur during material deposition by robotic welding, the interconnection of the study models through simulation, the characteristics of trajectory generation, the use of statistical data processing methods, the introduction of experimental data into the study models, the observation of the error sources and their gradual compensation, as well as the need to couple the complex, multi-physical phenomena, led to the orientation of the Doctoral Thesis towards theoretical, numerical and experimental research that will analyze in an original way, but in full agreement with the current trends, the proposed topic and to focus the study on the heat-affected zone. This area locally modifies the microstructural characteristics of the base material. For this reason, the heat-affected zone (ZIT) exhibits inferior mechanical characteristics compared to the base material, and there is a risk of cracks appearing and propagating.

The main and secondary research objectives (Os) were pursued on the basis of the ideas synthesized in the Doctoral Thesis, as well as research directions that are not fully covered by the existing literature in the field (Fig 2.6).
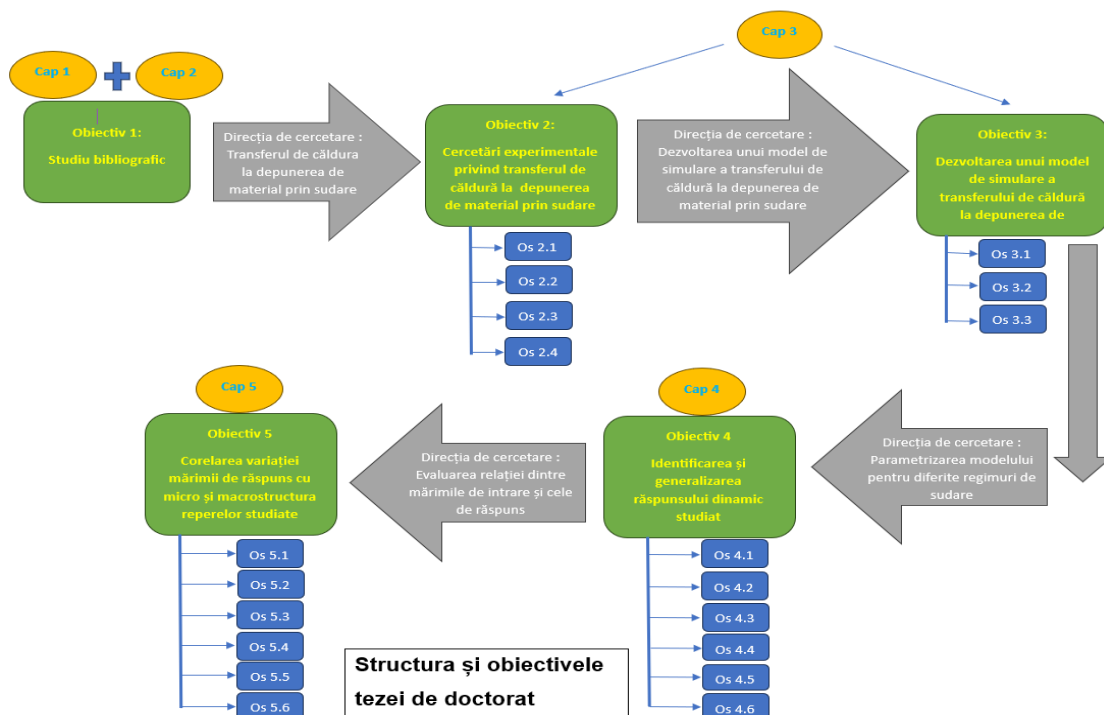

Fig 2.6. The objectives of the PhD. Thesis

A description of the research objectives and directions is depicted below:

- **Research Objectives**
  - **Primary Research Objectives**

- **OBJECTIVE 1**: A bibliographic study on the process of material deposition by robotic welding. The importance of experimental and simulation research on heat transfer at the base material level was highlighted on the basis of specialized literature.
- **OBJECTIVE 2**: Experimental research regarding the heat transfer that occurs during robotic surfacing welding. This objective involved the development of an experimental stand for the material deposition process, based on a series of samples and an experimental plan. A thermal acquisition system was used to capture the temperature gradient at the base material level during the process. The following secondary objectives are distinguished:
  - **Os 2.1:** Produce a sample based on the technology of material deposition by robotic welding, taking into account the parameters of the technological regime.
  - **Os 2.2:** Experimental processing of temperatures at the level of the external surfaces of the part using two distinct measurement ranges.
  - **Os 2.3:** 3D scanning of the welded part to transpose the real shapes of the external surfaces in digital form.
  - **Os 2.4:** Reconstruction of the surfaces of the 3D scanned model based on Reverse-Engineering techniques.

- **Objective 3: Development of a coupled CFD-FEM simulation model of heat transfer during material deposition by robotized welding.** This objective is based on the temperature variation over time at several locations in the base material. These were used both for the constraint of the heat flux in the solid domain and for the verification of the results obtained as a result of CFD-FEM simulations. A realistic representation of the geometry of the scanned part was included in the simulation. On the other hand, the computation model was designed to allow subsequent parameterization. In this way, the variation of the parameters of the welding regime can be taken into account. The following secondary objectives are distinguished:
  - **Os 3.1:** Development of a CFD simulation model to capture the interaction between the fluid medium (materialized by the flow of the shielding gas) and the solid medium (materialized by the outer walls of the welded part)
  - **Os 3.2:** Development of a FEM simulation model for the transient analysis of heat transfer due to the interaction between the base material and the filler material
  - **Os 3.3:** Coupling of the two simulation media to constrain the fluid domain (materialized by forced convection in CFD) and the heat

- **Objective 4: Identification and generalization of the dynamic response of the studied system.** The disadvantage of parametric CFD/FEM simulation models is the high computational costs. A method that allows the generalization of the dynamic response of thermal analysis is the use of first-order systems through transfer functions. For this, in the simulation model, the uniform variation of the temperature at the level of the weld bead footprint was considered. The temperature in the system was studied until it reached equilibrium. The time constant and the gain of the transfer function can be modified to take into account the variation of any technological regime parameter.
  - **Os 4.1:** Experimental study of temperatures outside the ZIT for several references considering the variation of gas flow.
  - **Os 4.2:** Parametric modeling of the initial simulation model to take into account the variation of gas flow in CFD analysis and temperatures at the level of the weld bead sections in FEM analysis
  - **Os 4.3:** Use of FOPDT systems to describe temperatures outside the ZIT during the process of material deposition by robotized welding

- o **Os 4.4:** Identification of the system's gain and time constant based on the Nishikawa step response method
- o **Os 4.5:** Making corrections to the initially determined constants based on experimental values
- o **Os 4.6:** Evaluation of the relationship between correction coefficients and gas flow for subsequent use
- **Objective 5: Correlation of the measured temperature variation with the micro and macrostructure of the studied plates.** The way in which heat transfer occurs during robotized material deposition welding directly influences the micro and macro structure of the base material. In this sense, studies by means of defectoscopy provide an important perspective on the relationship between the parameters of the welding regime, thermal transfer, and the quality of the weld.
  - o **Os 5.1**: Identification and determination of the number of drops, slag crusts, geometric irregularities, marginal craters, solid film deposits, weld bead widths, and weld bead heights following visual inspection
  - o **Os 5.2**: Determination of the geometric parameters (penetration and rise, joining angle, ZIT value measured in section at the surface and root of the plates) using an optical microscope
  - o **Os 5.3**: Calculation of dilution and linear energy for each plate
  - o **Os 5.4**: Evaluation of the linearity relationship between the measured values and the correction coefficients of the conductance and capacitance of the simulation model
  - o **Os 5.5:** Development of a multiple linear regression model to generalize the relationship between the geometric properties, microstructural defects, dilution, and correction coefficients k and τ
  - o **Os 5.6**: Verification of the generalization degree of the approach for specimens/plates that are outside the data set

Chapter 3. CFD-FEM modeling of the robotic surfacing weld heat transfer

3.1. Modeling stages

The purpose of this chapter is to develop a simulation model of heat transfer for robotized material deposition welding. This model was created in the ANSYS Workbench 19.0 environment.

In the first stage, the experimental part was established. The stand consists of a MIG/MAG robotized welding cell in which the necessary equipment for was integrated. The welded part represents a metal plate. The technological regime parameters are set in accordance with the base material and the specifications of the robotized system used.

The finished part was scanned in 3D to reconstruct the real shape of the outer surfaces in the CAD environment. In this sense, point clouds were processed using the SpaceClaim, and the preparation of the calculation model took place in the DesignModeler interface.

For the realization of the simulation model, two types of analyses were carried out: fluid flow (Computational Fluid Dynamics – CFD), and transient thermal analysis (Transient Thermal) respectively. The two simulation environments took into account the material characteristics, the way in which heat exchange takes place between the part and the ambient environment, and the properties of the protective gas.

The results of the CFD analysis were processed to identify the convection coefficient in relation to the torch position. This forced convection gradient was then used as input data in the thermal analysis. In this stage, the temperatures obtained from experiments based on infrared thermography were used to constrain the heat flux in each bead generation sequence.

The verification of the results of the thermal analysis was carried out by considering the variation of the temperatures at the level of an arbitrary location of the welded part. These temperature values were experimentally measured using a pyrometer.

Figure 3.1 illustrates the main steps of the proposed approach
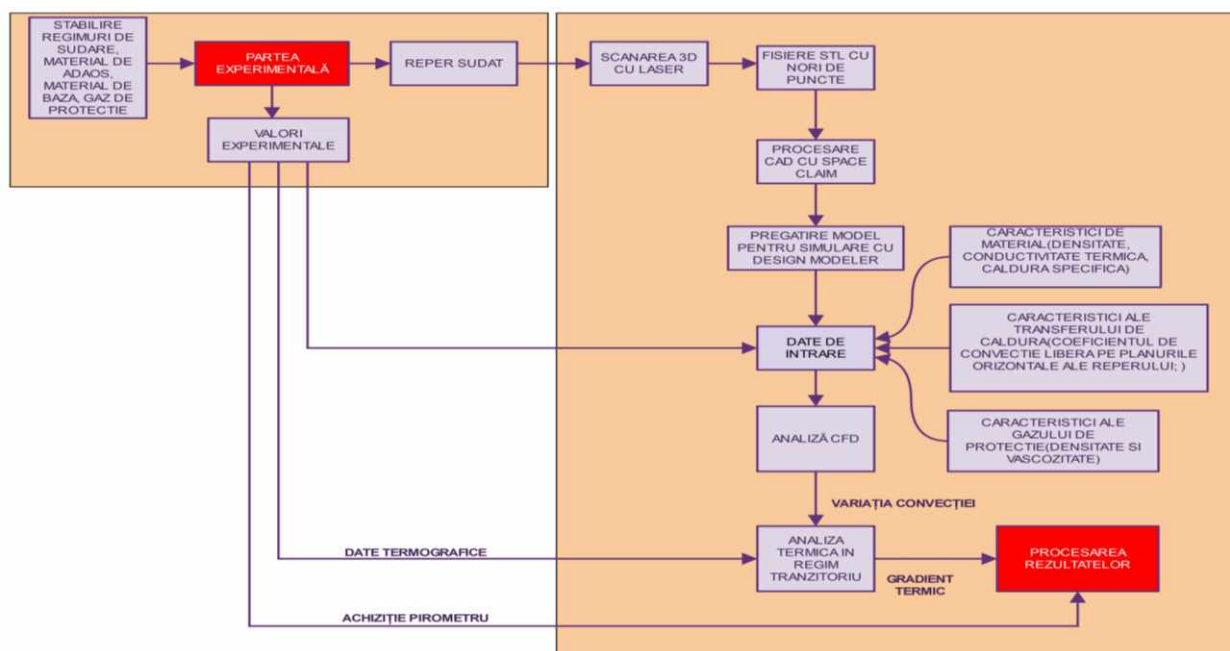
Fig. 3.1. The steps of developing a simulation model

3.2. Objectives

Chapter 3 follows two of the main objectives of the Doctoral Thesis:

- **OBJECTIVE 2:** Experimental research on heat transfer during robotized material deposition welding
- **OBJECTIVE 3:** Development of a simulation model of heat transfer during robotized material deposition welding

3.3. The experimental setup

The base metal

The plates on which material was deposited by robotized welding are 200 mm long, 100 mm wide, and 10 mm thick. They are made of S235JR steel, which is a type of carbon steel used in welded assemblies.

The shielding gas

The shielding gas is composed of 82% Argon and 18% Carbon dioxide. It is compatible with the chosen electrode wire and is suitable for material deposition welding operations of plates made of carbon steel.

The robotic cell

The robotized welding cell used is specific to this type of application and consists of:

- A Fanuc 100i B industrial robot equipped with a robotized welding gun (also known as a "welding torch") and a wire feed-and-push equipment.
- A controller.
- A perirobotic system with two workstations (a modular table on which the plate is fixed).
- A welding source.
- A torch management system (the system that maintains the gas nozzle).
- A gas cylinder.
- Intermediate systems (hose for transporting the shielding gas, electrical current elements).

The semi-finished product is positioned on the worktable of the perirobotic system. The trajectories necessary for generating the weld bead and the technological regime parameters are automatically performed by the information unit of the cell.

Figure 3.1 illustrates the physical components of the robotized welding cell and the layout of the temperature acquisition equipment."

Fig 3.1 The robotic welding cell: 1. Fanuc 100 iB Industrial Robot 2. Raynger MX4 Infrared Pyrometer 3. PC for data acquisition from the pyrometer, 4. Infrared camera, 5. Base metal, 6. Modular fixture

The first step was to ensure a suitable surface for the plates. For this purpose, the surfaces were prepared with an angle grinder and degreased with technical alcohol.

The second step was to ensure the identical positioning of the plates on the perirobotic system. Thus, the beads are made identically in length and position. This is ensured by the modular work table. It contains T-shaped channels that allow the fixing and positioning of the parts in the same place.

A third step was to program the robot to create the bead. This was done using the robot's training device in the following way: a characteristic point was created (a coordinate system positioned at the tip of the electrode wire of the effector); then the creation of the characteristic point of the marker (the coordinate system specific to the plates) followed; the trajectory to be followed by the robot was then defined, which represents the length of the weld bead, trajectory accompanied by the activation of the signal for the welding source and the shielding gas.

The gas flow was manually adjusted from the gas cylinder. The free length of the electrode wire was adjusted before welding with the help of a wire cutting tool. Only the current intensity and wire feed speed were changed from the teach-pendant. The other parameters were determined automatically.

Weld process parameters

Table 3.1 presents the main parameters of the welding process that are considered in the experiment. They were established on the basis of the recommendations of the work [172].

Table 3.1 Welding parameters

Parameter	Symbol	Value	Units of measurement
Gas flow rate	d_g	10	l/min
Intensity of the welding current	I	320	A
Voltage	U	31.7	V
Electrode wire feed rate	v_a	11	m/min
Welding speed	v_s	55	cm/min
Electrode stick out	L_l	20	mm

Temperature measurement system

During the experiments, the temperatures were measured with two acquisition systems, for two measurement ranges:

1. **Raynger MX4 pyrometer:** Ensures the measurement of temperatures from a location outside the material deposition area. It can measure temperatures between -50 and 800°C. The results of the acquisition are stored on a computer to be used in the process of verifying the results of the simulation model.
2. **FLIR SC640 thermal imaging camera:** This ensures the measurement of temperatures in the area of material deposition. The measurement range is up to 2000°C and allows the capture of the temperature at which the weld bead is generated. The acquired temperatures were stored on a computer to be used for the heat flux constraint in the thermal analysis. The two temperature acquisition instruments were necessary because the thermal imaging camera has a working range of [-40 °C… +2000 °C], but it can only operate in two ranges [-40 °C….+500 °C] and [500 °C … +2000 °C / +2300 °C]. Thus, the camera acquires temperatures during the experiments in the range [500 °C - 2000 °C / +2300 °C], and for the acquisition of the values below 500°C the pyrometer was employed. The SC640 camera is designed for non-contact measurement of temperature variations that occur at the level of the external surfaces of an object that is subjected to thermal loads. During the process, the camera was connected to a laptop where the images/video recordings were stored. They were then processed with the "ThermaCam Researcher" application. The purpose of the

measurement system is to capture the variation of temperatures along the bead. The Raynger MX4 pyrometer can measure without contact. The measurement takes place due to the transfer of heat by radiation. Therefore, the emissivity of the material was defined in the calibration phase (the same thing must be defined at the time of data processing and at the thermal imaging camera; in this case the emissivity was set to 0.8). Data acquisition is done via the serial interface. The measurement areas with the thermal imaging camera and the pyrometer, the geometric details and the position of the robotic welding torch are shown in Figure 3.2. "
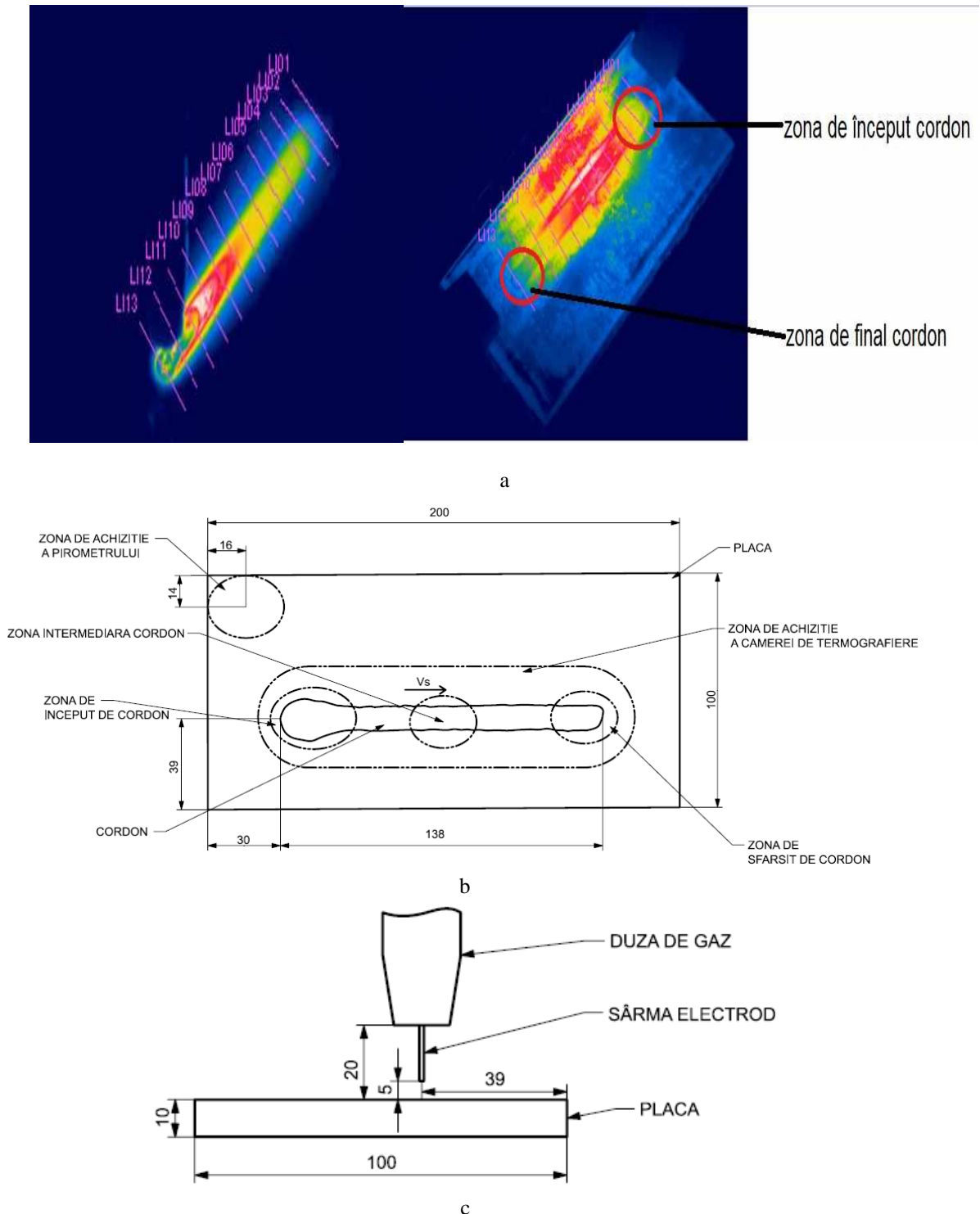

a

b

c

Fig 3.2 Details regarding the areas captured by the infrared camera (a) and the pyrometer (b) and (c)

Experimental results

Figure 3.3 illustrates the temperature variation with respect to time considering the initial, central and final position of the torch. The acquisition was performed through the thermal imaging camera. The measurement range is limited from 500 °C to 2000 °C / +2300 °C. Temperatures that exceed 1800°C (the steel evaporation temperature) were processed from the electric arc. These only occur for a fraction of second.
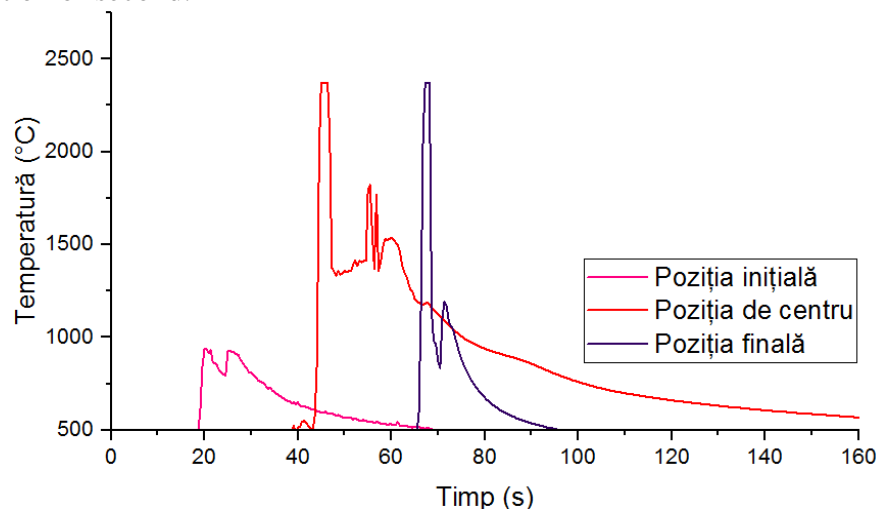
Fig 3.3 The change in the temperature in relationship with the acquisition time by using the infrared camera considering the initial, center and final position of the welding torch

Figure 3.4 presents the temperatures acquired with the support of the pyrometer
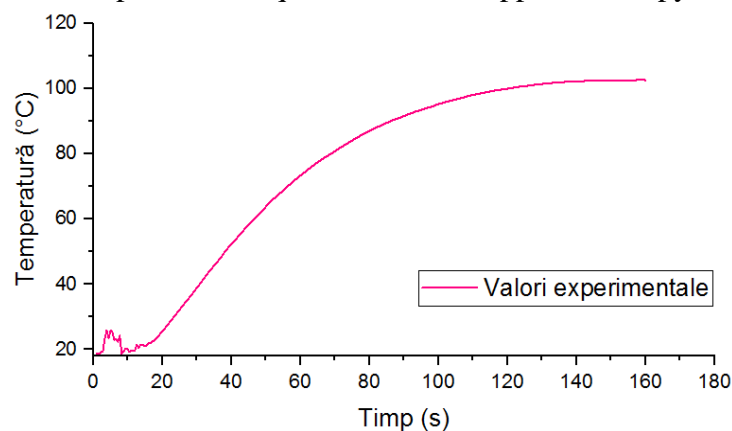
Fig 3.4 Temperature variations over time acquired using the pyrometer

3D scanning of the plate

The 3D scan of the plate was performed using the ABSOLUTE ARM 85 laser scanner. This scanner reconstructs the shape of the plate and the cord as a point cloud. The file is exported in "STL" format, which is then imported into the modeling program, in this case, ANSYS SpaceClaim.

Reconstructing geometry in the SpaceClaim interface

The transition from the point cloud generated by the 3D scan to CAD surfaces was done in SpaceClaim program.

3.4. CFD analysis of the protective gas flow

CFD is a branch of engineering that involves the study of fluid motion, thermal flow, and fluid-solid interactions. CFD can provide detailed information on the distribution of velocity,

pressure, temperature, or other relevant parameters in the fluid domain in transient or steady state regime [174].

The solid domain

The first step in creating the CFD simulation model is to translate the CAD model from the SpaceClaim interface to the DesignModeler one. After this transfer, a sum of surfaces is obtained that enclose triangular and/or rectangular edges. These are just an approximation of the physical geometry. The model reproduction strategy involves the sectioning of the cord with a step of 5 mm, resulting in 27 segments.

In the end, the 3D model from figure 3.5 is obtained. It has 28 solid bodies (one body for the base material and 27 bodies for the delimited segments of the weld bead).
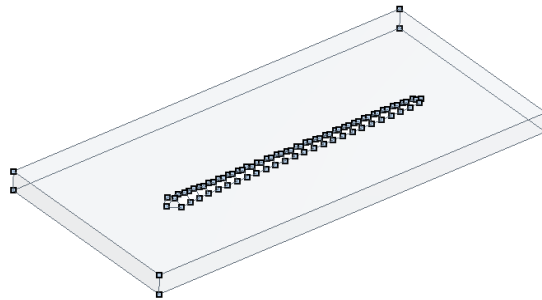
Fig. 3.5. Sampling of the weld bead

The fluid domain

For this type of analysis, the welding torch was included in the model. It was placed in the welding position, at a 90° angle to the surface of the plate, exactly as in the experiment.

In the next step, the torch was simplified by removing the components that do not materialize the fluid flow path. The representation of the flow domain is shown in figure 3.6.
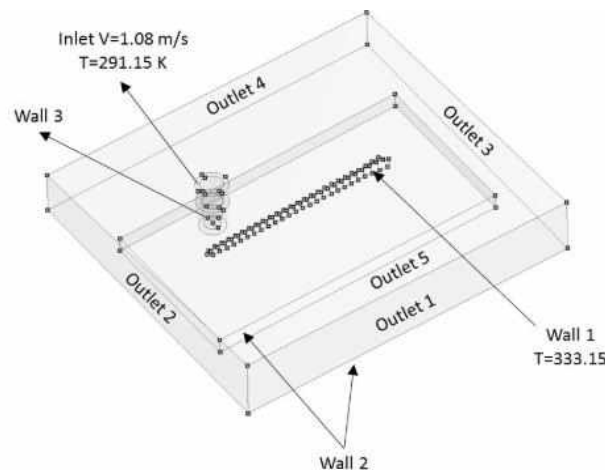
Fig 3.6 Details of the flow domain

Defining the simulation conditions

The CFD analysis was performed using the ANSYS CFX solver. The fluid inlet velocity was set at the gas nozzle. Considering that the Reynolds number of this problem is $1 \cdot 10^5 > 4000$ and the images aquired with the high-speed camera proved a turbulent flow regime, the k-epsilon turbulence model with the activation of the energy equations was employed to capture the temperature variation at the interface between the fluid and solid domain. The purpose of the

simulation was to process the temperatures adjacent to the weld bead. The calculated values are necessary for the interpolation of the forced convection coefficient on the outer surfaces of the plate.

Because the torch performed a translational movement equal to the welding speed, during the simulation the forced convection gradient will migrate with respect to the torch location. Therefore, 27 cases belonging to the 27 previouslydefined sections were analyzed.

The following input data were used for the simulation: molar mass, density, and specific heat of the shielding gas. Table 3.2 shows the values used.

Table 3.2 Shielding gas characteristics

Molar mass [Kg/Kmol]	Density [Kg/m^3]	Specific heat [J/Kg°C]
39,8	1,69	520

The flow rate of the shielding gas was evaluated based on the relationship:

$$v_g = \frac{d_g}{A} \tag{3.1}$$

Where: d_g represents the gas flow rate, and A represents the nozzle cross-sectional area.

For the current problem, the v_g velocity was 1.08 m/s, which corresponds to a flow rate of 10 l/min. The determination of the temperatures near the welding bead implies the definition of the initial temperature values for the 27 delimited segments. For this purpose, the experimentally determined temperatures were employed. For each increment of the welding torch displacement, the values of the forced convection coefficient were exported for the subsequent use in the transient thermal analysis.

Processing the results of CFD analysis

Figure 3.7 shows the convergence graph of the residuals for the mass and momentum equations. The decreasing trend of the values can be observed, with the RMS value being below $1 \cdot 10^{-5}$ after 100 iterations, indicating a normal convergence of the results after 100 iterations.
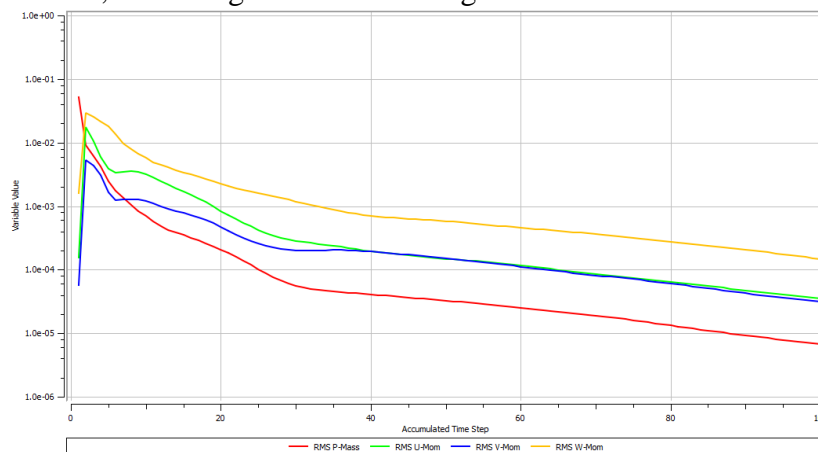

Fig 3.7 Monitoring the convergence of the results

- **The fluid velocity vector**

The representation of the flow lines of the protective gas provide information about how the gas moves in the studied space.

Figure 3.8 presents the velocity vector at the initial position of the torch. The maximum speed of 1.39 m/s occurs inside the nozzle, while speeds of 0.65 m/s occur at the interaction between the protective gas and the base material.
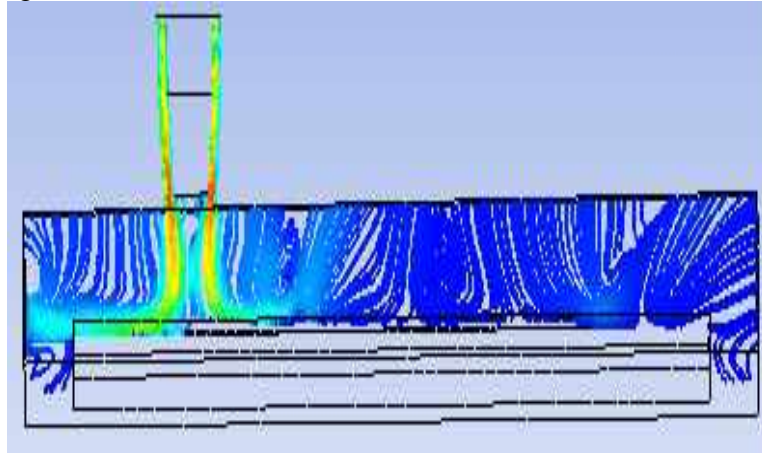
Fig 3.8 The fluid velocity vector at the initial position of the torch

Figure 3.9 shows the velocity vector at the final position of the torch. In this case, the gas flow tends to return in the initial space. However, the distance between the end of the bead and the edge of the reference is 35 mm, which disrupts the flow path. In this case, a recirculation trend occur, in which the gas velocity increases locally at the end of the bead and gradually decreases towards the edge of the part.
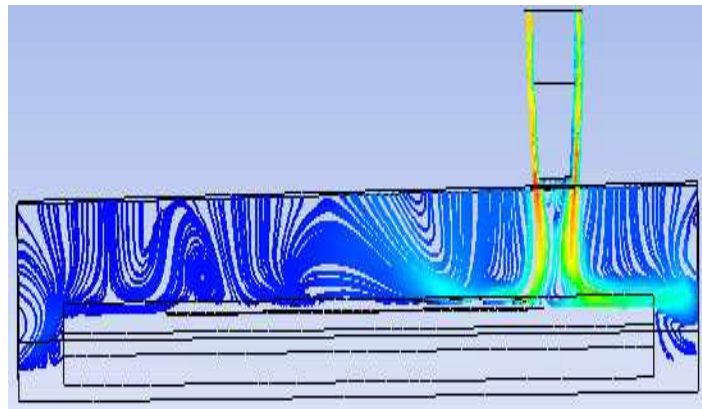
Fig 3.9 The fluid velocity vector at the final position of the torch

- **Forced convection coefficient**
    In the case of electric arc welding processes, heat transfer by convection is exhibited essentially due to the interaction between the reference and the ambient environment. Thus, a fraction of the thermal energy stored at the reference level is transferred to the ambient environment, facilitating the solidification of the deposited material. However, the rapid cooling of the welding bead is mainly influenced by the interaction between it and the protective gas. From the heat transfer point of view, the fluid flow rate leads to an increase in the convection coefficient (a measure of the transfer rate depending on the moving fluid). A realistic simulation of the process requires the processing of the temperature difference between the solid and fluid environment depending on the torch position. In this way, the value of the convection coefficient is known for

each increment of the torch position. Figure 3.10 shows the variation of the convection coefficient with respect to the torch position.
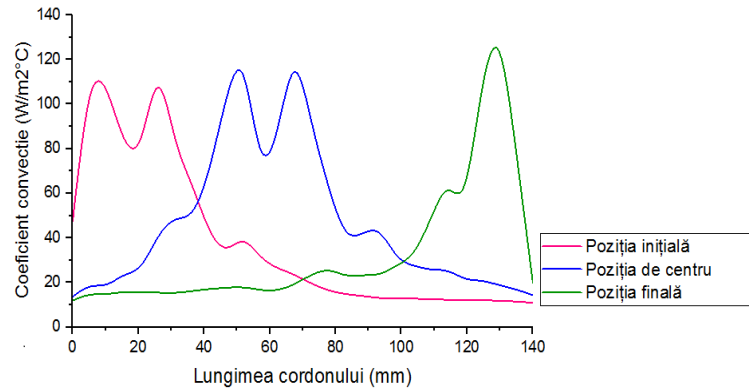
Fig 3.10 Variation of the convection coefficient with respect to the bead length considering the initial, final and center position of the welding torch

Three positions are considered: initial, middle and final. The maximum value of 125.3 W/m^2°C is exhibited in the final position of the torch. The maximum value can be explained on the basis of the recirculation zone visible when processing the velocity vector and the velocity gradient.

The variation of the forced convection coefficient is taken into account through CSV files. The transition from the fluid domain to the structural domain is carried out by suppressing the fluid domain and meshing the solid domain. In each node of the generated network, the closest value of the convection coefficient from the locations stored in the CSV file is searched, based on the node coordinates.

Figure 3.11 illustrates the variation of the forced convection coefficient with respect to the initial position of the torch. The maximum value of the forced convection coefficient is 111.2 W/m^2°C. This appears at the level of the deposited material.
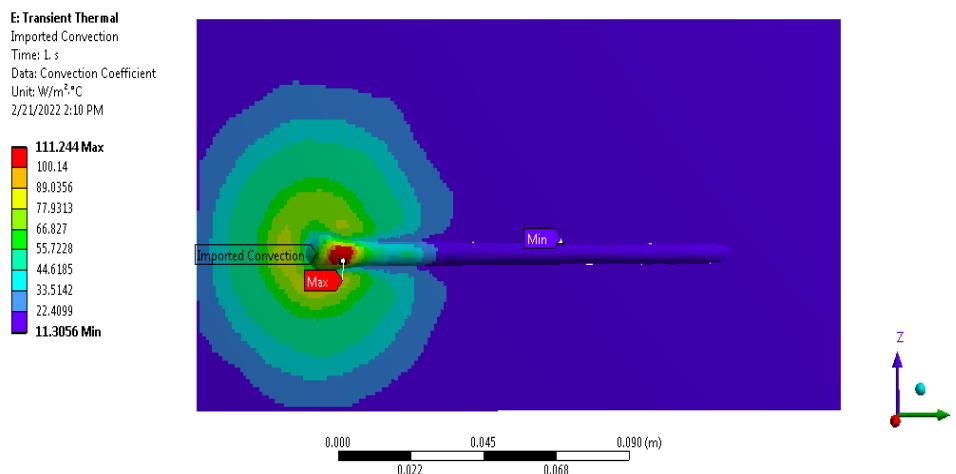
Fig. 3.11 Forced convection coefficient (W/m^2°C) at the initial position of the torch

Figure 3.12 shows the gradient of the forced convection coefficient with respect to the central position of the torch. The maximum value of the convection coefficient is 118.3 W/m2°C. This can be observed in several locations at the level of the bead. In this case, the effect of the real shape of the weld bead taken into account in the simulation model is visible. The variation of the forced convection coefficient value can also be explained by means of the velocity vectors.
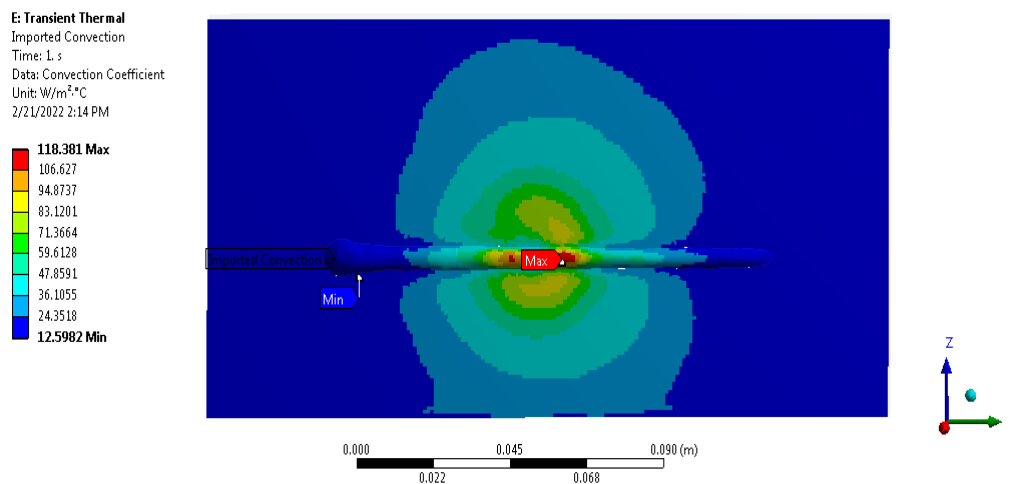
Fig. 3.12 Forced convection coefficient (W/m^2°C) at the center position of the torch.

3.5. Transient thermal analysis

Simulation conditions

The following conditions were defined in order to carry out the simulations:

- **Time step settings**

Taking into account the welding speed of 55 cm/min and the 5 mm segments of the bead, the simulation time was divided into equal steps of 0.55 seconds. In addition to the time steps required in the bead generation phase (approximately 14.8 s - the time required to create the bead on the plate), a cooling cycle of 145.2 seconds was also included in the simulation. This coincides with the time observed in experiments.

- **Temperature sttings**

In order to capture the temperature distribution in any location of the model, the temperature variations over time for each section of the weld bead were required. In this sense, the maximum temperatures of the deposited material at the level of each section defined by the bead were considered. The strategy involved processing the experimental results in the form of histograms. Locations where a discontinuity in the distribution of values appear were searched. Figure 3.13 shows an example for the middle section of the bead. The discontinuity between the temperature values indicatestemperatures that were captured only for a short period of time (the time when the temperature was > 1800°C). In this case, the values presented belong to the electric arc and must be filtered to ensure the relevance of the simulation results. The same procedure is performed for the entire bead.
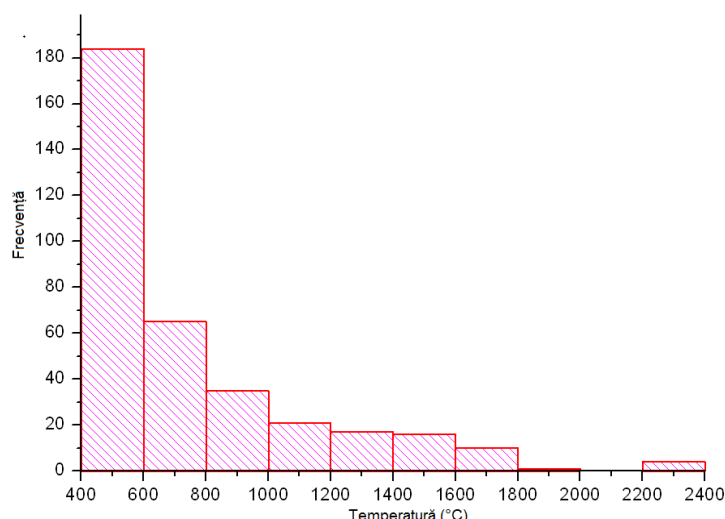
Fig. 3.13 Histogram of experimentally processed temperatures

Based on the study of the histograms, Table 3.3 shows the temperatures for the beginning, center, and end locations of the weld bead.

Table 3.3 Extract of temperatures from the simulation model

Torch position	Initial	Center	Final
Temperature [°C]	1708	1463	1188

- **Element activation/deactivation technique settings**

The "Birth and Death" technique allows the activation or deactivation of elements in the model to recreate the material deposition process. The technique is based on factors that multiply the values of the material properties (thermal conductivity in this case) which constrain the elements in a defined group to become adiabatic. During the simulation, each section of the bead is activated in accordance with the welding speed.

- **Forced convection sttings**

The forced convection evaluated in the CFD stage was exported to the FEA analysis. In this case, the import of gradients is done for each individual time step, depending on the position of the torch. For example, when section 1 of the bead is active, it appears in the simulation with a temperature of 1800 °C. In parallel, heat transfer by forced convection takes place considering the initial position of the torch from the CFD analysis. After the welding cycle is completed, cooling takes place under the effect of free convection, considering the horizontal plate theory.

Processing the FEM analysis results

The results that can be processed in the case of transient thermal analysis are the variation in time of the total heat flux and the temperature distribution.

The graphical representation of the temperature distribution for the final torch position is shown in Figure 3.14. In this case, the material was deposited over the entire weld length. The maximum temperature of 1188 °C remains concentrated at the end of the bead. The sphere of thermal influence becomes distinct in the interaction zone. Progressive cooling of the benchmark is observed, with processed temperature values around the bead being 280 °C.
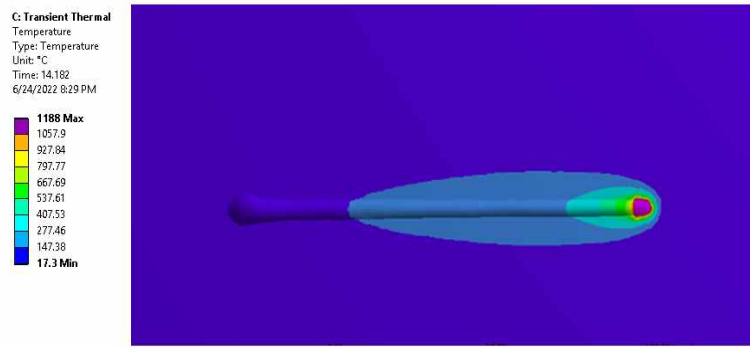
Fig. 3.14 Temperature distribution at the final torch position

Temperature gradients on the outer surfaces of the welded benchmark can also be processed based on infrared thermography. However, the relevant results for the analysis are the temperatures in the model section. This visualization method is important to obtain a deeep understanding of the thermal behavior of the analyzed system and the influence of different variables on it. This way, temperature concentration zones can be detected and potential thermal problems, such as hot spots or areas where insufficient cooling takes place, can be identified. The visualization of the section results also allows the evaluation of the thermal dynamics and the identification of temperature changes in deapth and within a certain time interval.

Table 3.4 presents the visualization of the results for different sections of the bead. The cooling sequence under the effect of convection is considered in two cases: immediately after the completion of the welding cycle ($\Delta t = 17.05$ s) and at the end of the cooling cycle ($\Delta t = 160$ s).

Table 3.4 Excerpt on temperatures from the simulation model

Cross section view	Top view
After the welding cycle is completed	
After the cooling cycle is completed	

The two cases illustrate how heat transfer is achieved in the depth of the material. This is closely related to the ZIT, which is thus numerically identified as a characteristic of the robotized material deposition welding process.

Validation of simulation model

Validation of the simulation model encompasses comparing the simulation results with those obtained from the experiments. Figure 3.15 shows the graph of the temperature variation measured by the simulation vs. those obtained by pyrometer.
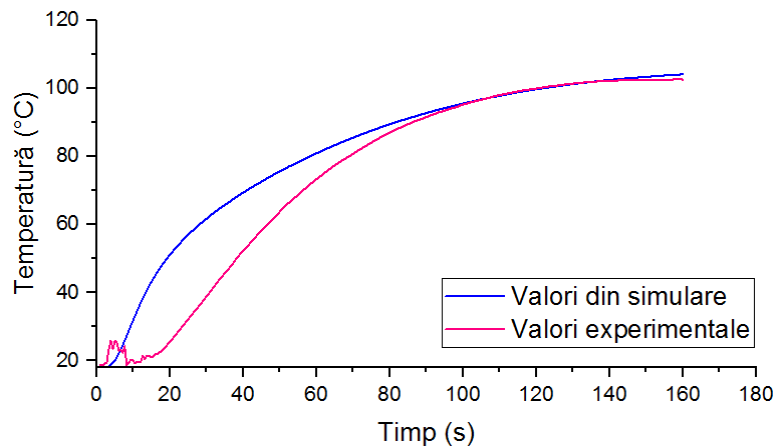
Fig 3.15 Comparison between simulation results and experimental data

To evaluate the accuracy of the simulation model, it is necessary to perform a statistical comparison of the two curves using MATLAB Simulink environment. In this regard, the experimental and simulation results are imported in CSV format for further processing (Fig. 3.16).
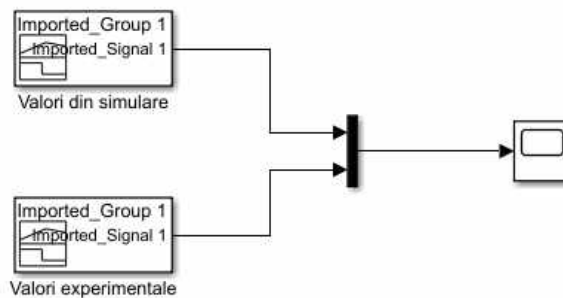
Fig 3.16 Processing of measured and calculated temperatures in MATLAB Simulink

Data is imported through two signal generator blocks (Imported Signal). The concatenation of these signals for the representation in a single graph is possible through the use of a multiplexer block (MUX). At the output, a block is employed for the graphical visualization of the two curves (Scope). This gives the possibility of statistical analysis of the signals, the relevant ones being:
• Max: the maximum temperature value recorded on the ordinate; • Min: the minimum temperature value recorded on the ordinate; • Peak to Peak: the difference between the minimum and maximum temperature; • Mean: the average of all values; • Median: the median of all values; • RMS: the root mean square error.

Figure 3.17 illustrates the statistical analysis of the experimental curve.
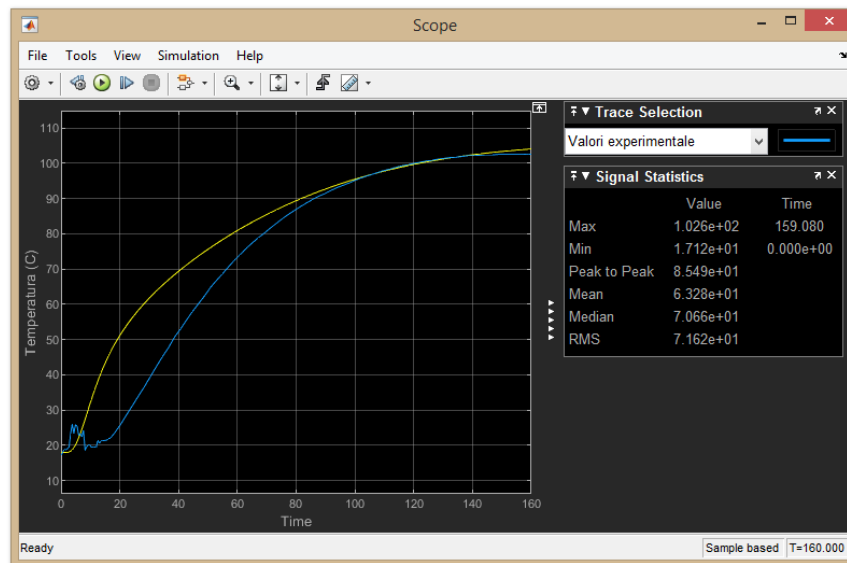
Fig 3.17 Statistical analysis of the signals in MATLAB Simulink

The simulation model can predict the maximum temperature from the pyrometer measurement location with high accuracy ($\varepsilon = 2.11\%$). However, a significant difference can be observed in terms of the stabilization time, which is confirmed by the median error of 11.08%.

3.6. Conclusion

The simulation model was validated by comparing the simulation temperature curve with the one obtained from experiments. The statistics of the two signals were interpreted using MATLAB Simulink. The graphs indicated a good match at thermal equilibrium ($\varepsilon = 2.11\%$ in the case of the maximum value). A difference of 4.8% in the minimum values are due to the noise in the experimental data (visible in the first 15 seconds, due to the electromagnetic interference generated by the ignition of the electric arc).

However, an error of 11.08% in the system stabilization time is observed. This can be explained by the fact that the model does not take into account the temperature-dependent material characteristics (this information is not provided by the manufacturer). Therefore, the dynamic response correction can be achieved by adjusting the system capacity.

Although the simulation model has been validated for a set of parameters, the goal of the research is to generalize it by considering different gas flow regimes. At the same time, it is also important to improve the dynamic response of the simulated system by reducing the stabilization time error. These aspects are analyzed in Chapter 4.

Chapter 4. The influence of gas flow variation on heat transfer in robotic material deposition welding

4.1. Introduction

The goal of this chapter is to study the influence of gas flow variation on heat transfer in robotic material deposition welding. The starting point is the previously developed simulation model. It must be parameterized to take into account different values of the input variables. In this

study, the geometry of the bead, the temperatures of its segments and the gas flow are taken into account. At the output, the temperature variation in a location outside the ZIT is captured.

Following the entire modeling - simulation flow described in Chapter 3 is inefficient in terms of the involved computer resources. This is mainly due to the Reverse Engineering process for reconstructing the geometry and the large size of the result files.

To compensate for the potential sources of error such as: the disregard of temperature-dependent material properties, or the idealization of the interaction between bodies, corrections have been done to the capacitance and conductance at the interface by employing concentrated parameters and the theory of first-order systems with delay (FOPDT). In this sense, the system's response to a step signal was studied to identify a transfer function described by a single pole.

In the next step, successive changes were done to the model's amplification factor and time constant until a good match was obtained between the simulated and the measured temperature curves. The graphical representation of these coefficients vs. gas flow allowed the generalization of the established dependency relationship for further use in any practical case.

Figure 4.1 illustrates the main steps of the proposed approach.
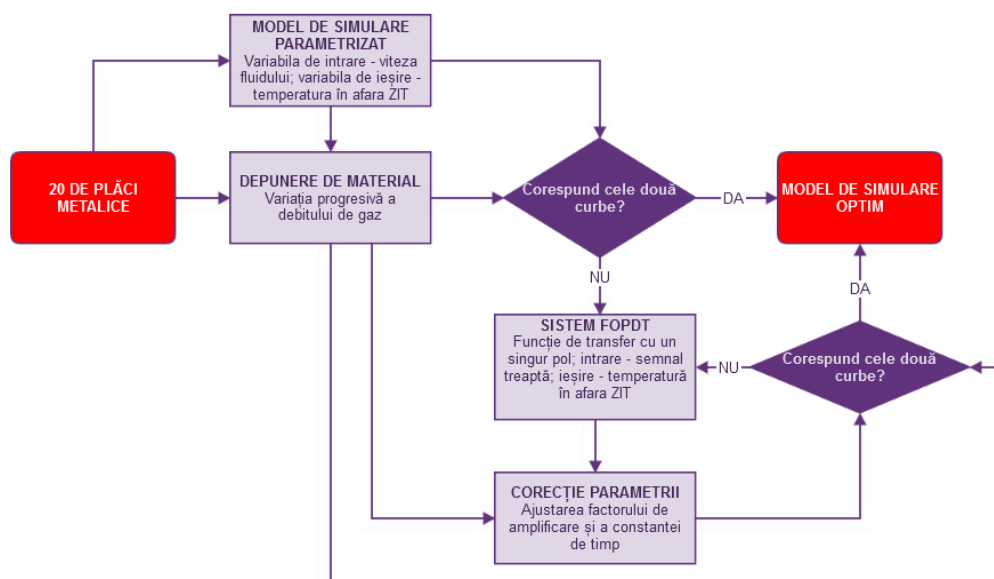
Fig. 4.1. The steps of developing a parameterized simulation model

4.2. Objectives

Chapter 4 follows the fourth objective of the Doctoral Thesis:

- **OBJECTIVE 4:** Identification and generalization of the thermodynamic response of the studied system

4.3. Experimental research on the influence of gas flow variation on heat transfer

The experiments were carried out by setting the welding parameters for each set of plates on which the material was deposited by the robotic welding. The following parameters were considered constant, while the gas flow rate (d_g) was gradually increased with the values of 10 l/min, 13.5 l/min, 17 l/min, 20.5 l/min, 24 l/min for set 3, and for sets 4,5,6,7,8 with the values of

10 l/min, 17 l/min, 24 l/min: • Current intensity (I); • Voltage (U); • Welding speed (v_s); • Electrode diameter (de); • Electrode wire feed speed (v_a); • Free length of the electrode wire (lcl);

Process parameters

Table 4.1 illustrates the technological process parameters for six sets of plates.

Tabel 4.1 Process parameters

Parameters	Set					
	Perpendicular torch		Torch inclined at 15°			
	3	4	5	6	7	8
I [A]	190	320	160	280	190	320
U [V]	18,9	31,7	17,7	29,2	18,9	31,7
v_s [cm/min]	45	55	45	55	45	55
d_e [mm]	1,2					
v_a [m/min]	4,7	11	3,9	9	4,7	11
l_{cl} [mm]	15					

Description of the experimental procedure

The experimental procedure is identical to the one presented in Chapter 3.

Set 3 includes 5 plates, providing an extended database for the behavior of the analyzed system. Additionally, errors or uncertainties associated with the results can be more precisely quantified, and the factors of influence and trends in the variation of temperature curves can be better highlighted.

Temperature variation curves

The results of the temperatures measured with the Raynger MX4 pyrometer are shown in Figure 4.2 for the 6 sets of the studied benchmarks.

Figure 4.2 presents the temperature variation curves for the set 3 of plates (denoted as Pl 7 to Pl 11).
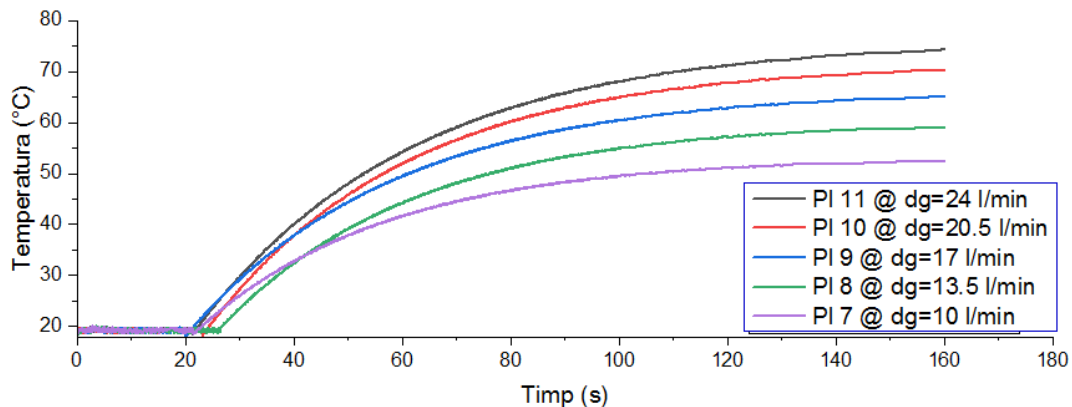
Fig. 4.2. Temperature curves obtained for the set 3 of plates (Pl 7 – Pl 11)

The study was continued using the system theory and the following characteristics were comparatively presented for each plate in the set: • Peak: Represents 2% of the maximum temperature value; • Rise Time: Represents the time interval necessary for the system response to

pass from the ambient temperature to 90% of the peak value; • Settling Time: Represents the time interval necessary for the system response to approach its final value by 2% after an input disturbance. In this case, the disturbance was induced by the welding cycle.

.

Based on the analysis of the dynamic behavior of the temperature curves studied using MATLAB software, the following conclusions can be drawn:

- The variation of the gas flow rate during the robotic welding material deposition process leads to a linear increase of the temperatures (T), according to the following relationships:
    - o Set 3: $T = (1{,}56 \cdot d_g) + 22{,}5$
    - o Set 4: $T = (3{,}33 \cdot d_g) + 25{,}09$
    - o Set 5: $T = (0{,}42 \cdot d_g) + 24{,}06$
    - o Set 6: $T = (1{,}4 \cdot d_g) + 50{,}59$
    - o Set 7: $T = (0{,}34 \cdot d_g) + 30{,}8$
    - o Set 8: $T = (0{,}58 \cdot d_g) + 76{,}5$

- The variation of the gas flow rate during the robotic welding material deposition process leads to the linear increase of the stabilization times (t_s) according to the following relationships:
    - o Set 3: $t_s = (4{,}10 \cdot d_g) + 97{,}7$
    - o Set 4: $t_s = (0{,}83 \cdot d_g) + 167$
    - o Set 5: $t_s = (0{,}34 \cdot d_g) + 139$
    - o Set 6: $t_s = (1{,}55 \cdot d_g) + 186$
    - o Set 7: $t_s = (1{,}56 \cdot d_g) + 22{.}5$
    - o Set 8: $t_s = (1{,}92 \cdot d_g) + 148$

Consequently, the heat transfer in the robotic welding material deposition process is influenced by the shielding gas through a proportionality relationship that exists between the flow rate and the dynamic characteristics of the temperature curves. The study highlights the fact that this condition is generally valid, regardless of the technological regime parameters or the mode of the filler material transfer.

4.4 Parametrization of the simulation model

The simulation model presented in Chapter 3 of the PhD Thesis was employed to parameterize the geometry and fluid velocity (as input variables) and the temperature time evolution (as response variable). Although this procedure can be performed directly in ANSYS Workbench interface, a number of original modeling and parameterization features were introduced in the PhD Thesis. These are described below.

Parametrization of the geometric model

Parametric modeling of the geometric model involves extracting the shape of the surfaces of the cross-sections of 27 segments into which the welding bead is divided (Fig. 4.3). The resulting surfaces are characterized by the area (s) which is constrained by the scale factors in the transversal and radial direction (a and b). These can be defined as parameters in DesignModeler interface. The connections between the sections can be done on the basis of 3D curves (c). The points that define the ends of the curves belong to the scaled surfaces. The reconstruction of the solid body on the basis of the surfaces and curves allows the entire parameterization of the welding bead. Thus, it can be scaled to properly respect the dimensions obtained from the 3D scans for each studied case.
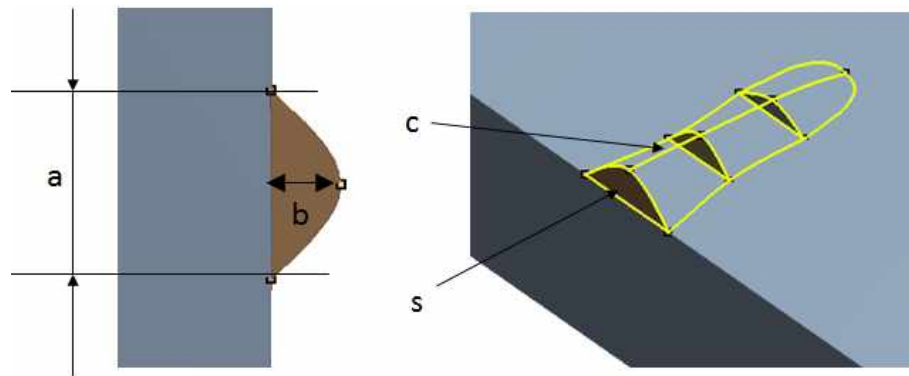
Fig. 4.3. Parametric representation of the surfaces that define the welding bead

Figure 4.4 illustrates an example of a parametric reconstruction of the welding bead. The model belongs to set 4 – Pl 12.
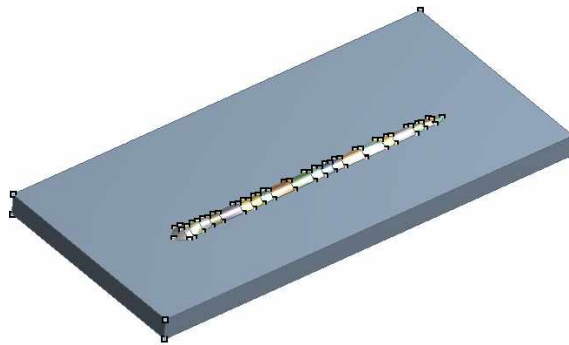
Fig. 4.4. Geometric model after the parameterization for set 4 - Pl 12

Parameterization of the fluid velocity

Direct parameterization of the model in ANSYS CFX interface is not possible due to the CFD-FEM transfer strategy for the convection coefficients in tabular format. That is why the use of an alternative strategy is required. For this purpose, a variation study was carried out with the aim of progressively increasing the gas velocity in the simulation model and graphically representing the variation of the convection coefficient in different positions of the torch (Fig. 4.5).
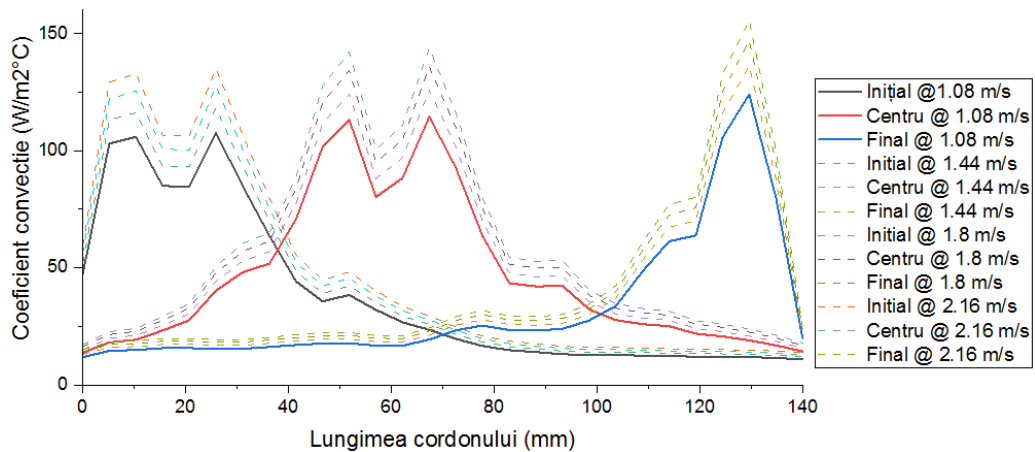
Fig. 4.5 Variation of the convection coefficient with flow rate

The study highlights the fact that the gas flow path is not influenced by the gas velocity. On the other hand, it can be observed that the value of the convection coefficient varies according to a polynomial law (Fig. 4.6).
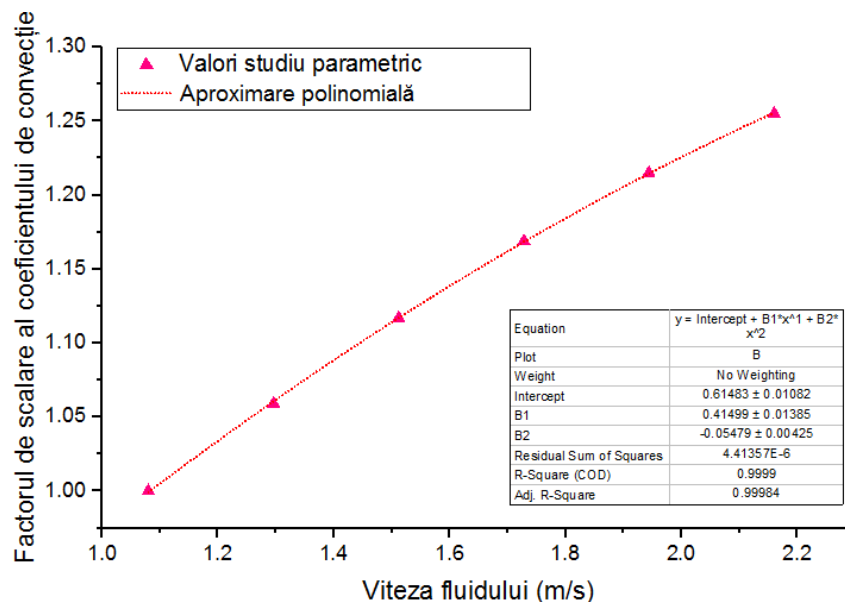
Fig. 4.6. Variation of the convection coefficient with gas velocity

The law can be described by the relationship:

$$h = -0{,}0643 \cdot v^2 + 0{,}449 \cdot v + 0{,}585 \tag{4.1}$$

Where h represents the convection coefficient at any location in the model and v the fluid velocity.

Verification of the simulation model

After the parameterization of the simulation model, the results obtained for the set 3 of the welded reference points were verified.

Figures 4.7 a and b show the differences between the temperature variation graphs obtained by simulation and measured temperatures with the pyrometer for plates 7 and 8 of set 3.
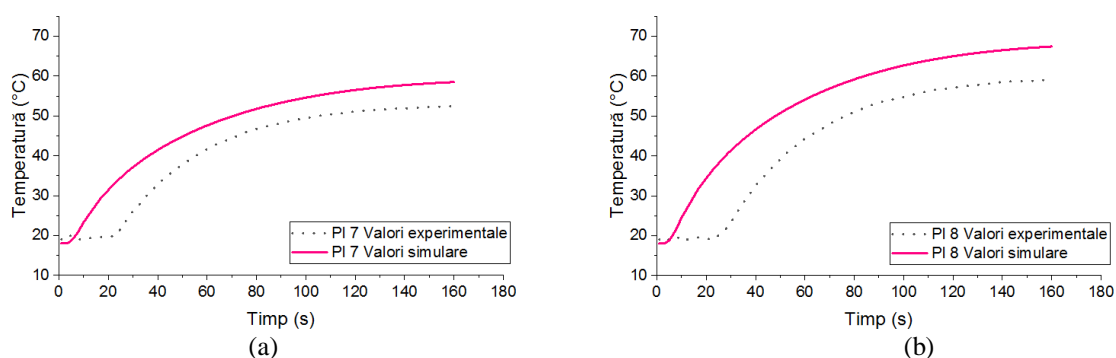
Fig. 4.7. Variation of the calculated and measured temperatures for set 3, Pl 7 and Pl 8

The dynamic characteristics of the curves obtained for the two plates are presented in Table 4.2

Table 4.2 Dynamic system characteristics for set 3 Pl 7 and Pl 8

Characteristic	Pl 7			Pl 8		
	Experiments	Simulations	Δ [%]	Experiments	Simulations	Δ [%]
Peak [°C]	37,44	27,00	27,88	43,97	33,00	24,95
Rise time [s]	75,14	35,99	52,10	86,12	41,43	51,90
Settling Time [s]	133,79	64,09		153,35	73,76	

Although the shape of the curves is similar, there is a significant difference between the temperatures and the dynamic characteristics of the curves obtained by simulations and the measured ones. The maximum difference between the peak values is 27% for plate 7, while the stabilization and rise times differ by 51.8% and 52.7%, respectively, for all cases.

In a generalized model, the errors detected in this study gathered with those presented in Chapter 3 of the Doctoral Thesis, requiring the finding of compensation strategies.

Theoretical explanation of the error sources

The temperature difference that occurs due to the variation of the gas flow in the case of electric arc welding can be explained by the theory of heat transfer by convection.

The variation of the shielding gas flow leads to an increase in the pressure exerted on the deposited material during welding. This eliminates micro-gaps and ensures a stronger contact between the base material and the filler material. Therefore, the thermal resistance decreases while the amount of heat transferred to the filler material increases.

4.5. Use of the first-order systems

Thermal systems include elements that can accumulate and transfer significant amounts of energy at a finite rate. In system theory, their modeling can be achieved by using first-order systems. [181]. Such differential equations can provide a simplified, but sufficiently accurate, description of the thermal response, based on a single input and output variable. For example, the heat flux due to the welding process is the input to the system, while the temperature variation over time represents the response.

The differential equation that connects the R(s) input value and the C(s) output value can be described in the frequency domain as [182]:

$$\frac{C(s)}{R(s)} = K \cdot \frac{1}{\tau s + 1}$$

(4.2)

Where: K represents the gain factor and τ the time constant of the system.

In the case of thermal systems, the constants in equation 4.2 are closely related to the material properties. For example, the thermal conductivity constrains the equilibrium temperature, which is directly proportional to the gain factor. On the other hand, the time constant can be correlated with the specific heat. Together with the density of the material, it determines the time it takes for the system to reach the equilibrium.

Simulation conditions such as the applied loads can be controlled based on the amplitude of the input signal. Knowing the initial values of the system, the parameters can be varied to perform studies without having to solve the equations corresponding to the transient thermal analysis. The objective is to determine the corrections applicable to the simulation model so that it can realistically reproduce the heat transfer evaluated by experiments.

In the case of transient thermal analysis, the constraint of the heat flux due to the interaction of two bodies can be achieved by using one-dimensional elements. These connect the nodes of the surfaces in contact and allow the limitation or improvement of the transfer due to the conduction, based on the theory of thermal resistances [183]:

$$q = R_{th} \cdot (T_i - T_j)$$

(4.3)

Where: q represents the heat transferred between the nodes of the element, R_{th} the thermal conductivity, $T_{i,j}$ the nodal temperatures.

In this way, by knowing the difference between the experimental gain constant and the one obtained after the simulations, the interface conductance correction can be performed.

On the other hand, the difference between the experimentally determined time constant and the one resulting from the simulations can be corrected by using capacitance elements. In this model the specific heat matrix is written in the form:

$$\left[C_e^t\right] = \left[C_{th}\right]$$

(4.4)

Where: C_{th} represents the thermal capacitance.

Another target of the capacitance elements is to impose the delay in the system response. In the case of thermal analysis, the delay due to the acquisition system is considered negligible. Given that the pyrometer has a certain sampling rate, it is necessary to include the dead time in equation when processing the experimental values, resulting a first-order system with delay [184]:

$$\frac{Ke^{-\theta s}}{\tau s + 1}$$

(4.5)

Where θ represents the system delay.

Identification of system constants

An important step in approximating the simulation model by a first-order delayed system is the identification of the constants K, τ and θ for each studied case. In this purpose, the Curved Surface Method proposed by Nishikawa [185] is employed. Figure 4.8 presents the location delimited by the two surfaces (A0 and A1) in the case of set 3, plate 11.
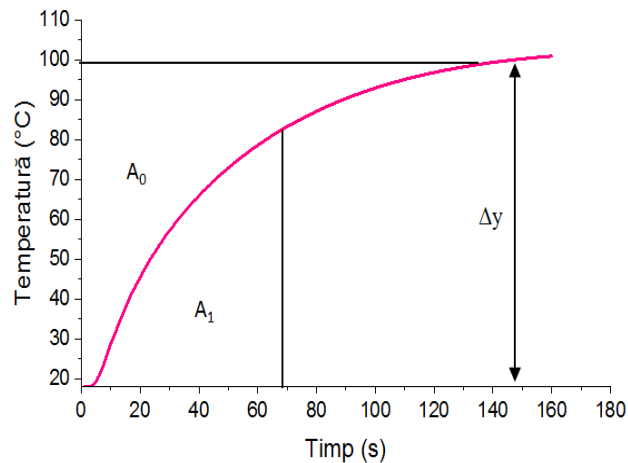
Fig. 4.8. Representation of the surfaces necessary for the system identification using the Nishikawa method

According to the symbols in figure 4.8, the calculation relationships are [185]:

$$A_0 = \int_0^\infty \left(\Delta y(\infty) - \Delta y(t) \right) dt \tag{4.6}$$

$$A_1 = \int_0^{t_0} \left(\Delta y(t) \right) dt \therefore t_0 = \frac{A_0}{\Delta y(\infty)} \tag{4.7}$$

Therefore, the constants of the first-order system can be evaluated based on:

$$k = \frac{A_1}{0,368 \Delta y(\infty)} \tag{4.8}$$

$$\theta = t_0 - \tau \tag{4.9}$$

The accuracy of the model is verified based on the mean squared error [186]:

$$M = \frac{1}{n} \sum_{t-1}^n \left| \frac{A_t - P_t}{A_t} \right| \cdot 100 \tag{4.10}$$

Where A_t is the current value, P_t is the predicted value, and n is the number of plates.

The algorithm was implemented in MATLAB. In the first step, the working variables are defined. These are imported into the work environment in the form of vectors, with the following symbols: t for the time step, u - the amplitude of the step signal at the system input, and y - the experimental temperature value for each time step.

Table 4.3 shows the values of K, θ and τ obtained after processing the measured temperatures for the 5 plates belonging to set 3. The mean squared error (M) is calculated based on the step response of the system reported to the initial values.

Tabel 4.3 Amplification factor, delay and time constant for set 3 measured temperatures

Plate	K	θ	τ	M[%]
7	57,5	21,1	37	0,45
8	53,2	23,1	32,8	0,46
9	48	20,1	27,5	0,51
10	41,8	25,1	25,9	0,39
11	34,9	21,1	24,5	0,32

The same results are processed in table 4.4 considering the variation of temperatures over time for the 5 plates, obtained after the parameterized study.

Tabel 4.4 Amplification factor, delay and time constant for simulated temperatures set 3

Plate	K	θ	τ	M
7	85,93	4,2	74,57	0,32%
8	73,72	4,2	59,43	0,33%
9	62,51	4,2	49,38	0,33%
10	52,42	4,2	40,68	0,32%
11	43,50	4,2	33,31	0,32%

Evaluation of necessary corrections

The difference between the errors of the first-order system constants determined experimentally with Nishikawa, and those obtained by processing the simulations with Nishikawa are presented in table 4.5.

Tabel 4.5 Error between experimental and simulation first-order system constants

Plate	Error [%]		
	K	θ	τ
7	49,44	80,09	101,54
8	38,57	81,82	81,19
9	30,23	79,10	79,56
10	25,41	83,27	57,07
11	24,64	80,09	35,96

The compensation of these errors can be achieved by determining correction coefficients, based on the relationships:

$$C_K = \frac{k_{\text{experimental}}}{k_{simulare}}; C_\theta = \frac{\theta_{\text{experimental}}}{\theta_{simulare}}; C_\tau = \frac{\tau_{\text{experimental}}}{\tau_{simulare}}$$ (4.11)

Where: C represents the correction coefficients. The results obtained are presented for each welded plate of set 3 in table 4.6.

Tabel 4.6 Calculated correction coefficients

Plate	Correction coefficient		
	C_K	C_θ	C_τ
7	0,67	5,02	0,50
8	0,72	5,50	0,55
9	0,77	4,79	0,56
10	0,80	5,98	0,64
11	0,80	5,02	0,74

Generalization of the correction coefficients

The generalization of the correction coefficients involves adapting them to compensate for the errors that occur between the simulation model and the real behavior of the material deposition process through robotic welding for any current intensity and gas flow values.

The graphical representation of the correction coefficients for the amplification factor K vs. gas flow is illustrated in Figure 4.9.
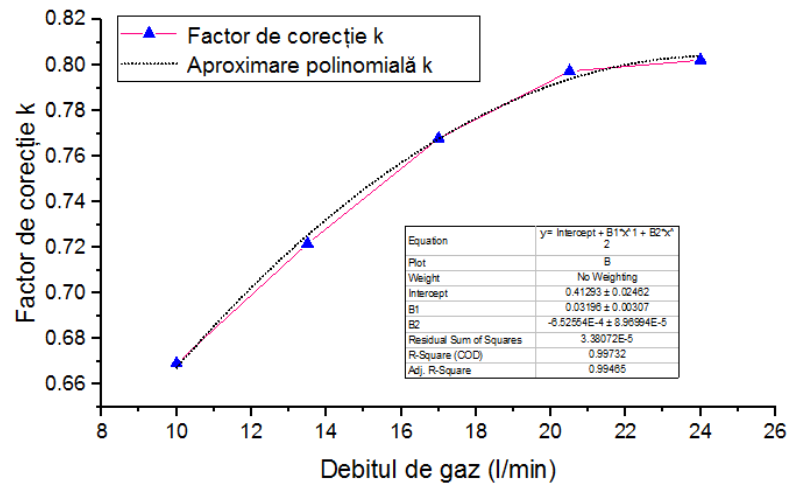
Fig. 4.9. The graphical representation of the relationship between the correction coefficient for K and the gas flow rate

After the graphical representation of the correction factors for K, the polynomial regression trend is observed. For their approximation, a 2 degree function can be used:

$$C_k = -0,0007 \cdot d_g{}^2 + 0,032 \cdot d_g + 0,4129 \qquad (4.12)$$

A linear approximation can be employed to evaluate θ values:

$$C_\theta = 0,0136 \cdot d_g + 5,03 \qquad (4.13)$$

The curve for the correction factor of θ are in polynomial regression, and can be described by the following relationship:

$$C_\tau = 0,0009 \cdot d_g{}^2 + 0,0158 \cdot d_g + 0,57 \qquad (4.14)$$

In equations 4.12 - 4.14, the variable is represented by the gas flow rate. To generalize the relationship for another parameter of the welding regime, the constants are expressed in terms of the welding current intensity.

Thus, in the case of the correction factor for K, equation 4.12 can be rewritten as:

$$C_k = -\frac{0,13}{I} \cdot d_g{}^2 + \frac{6,08}{I} \cdot d_g + \frac{78,45}{I} \qquad (4.15)$$

By giving a common factor the ratio between the flow and intensity, the result is:

$$C_k = \frac{d_g}{I} \cdot \left(-0,13 \cdot d_g + 6,08 + \frac{78,45}{d_g} \right) \qquad (4.16)$$

In a canonical form, equation 4.15 can be written as:

$$C_k = \frac{1}{I} \cdot \left(-0,13 \cdot d_g{}^2 + 6,08 \cdot d_g + 78,45 \right) \qquad (4.17)$$

Similarly, in the case of the time constant:

$$C_\tau = \frac{1}{I} \cdot \left(0,17 \cdot d_g{}^2 + 3 \cdot d_g + 108,32 \right) \qquad (4.18)$$

The methodology presented is applicable exclusively to first-order systems with delay. However, it is necessary to correlate the values of the constants K, τ and θ for including the correction factors in the simulation model. In this sense, FEA employs one-dimensional thermal conductivity and dimensionless elements for capacitance. Thus, a simulation model is developed on which the sensitivity of the model and the heat transfer can be studied when including correction elements in the transient thermal analysis.

In the first step, the contact between the weld bead and the reference is replaced with 1D elements. The nodes located on the separation plane will exchange the heat based on the principle of thermal resistances. On the other hand, the nodes corresponding to the area where data is acquired by the pyrometer are associated with a 0D element of "thermal mass" type.

This will impose both an initial delay of the system, and the time it takes to reach the equilibrium state. On this model, a parameterized study was carried out to evaluate the initial values of the thermal conductivity. To this end, the temperatures imposed at the level of the bead were set to 1°C, while the ambient temperature was considered 0°C. Heat transfer is done only by conduction and free convection. The simulation time was extended to 1600 seconds.

Figure 4.10 shows the results obtained for the thermal conductivity values (denoted with TCC) ranging from 900 to 4500 W/m²°C. It was observed that the equilibrium temperature of the system no longer varies at values of conductivity over 3600 3600 W/m²°C.
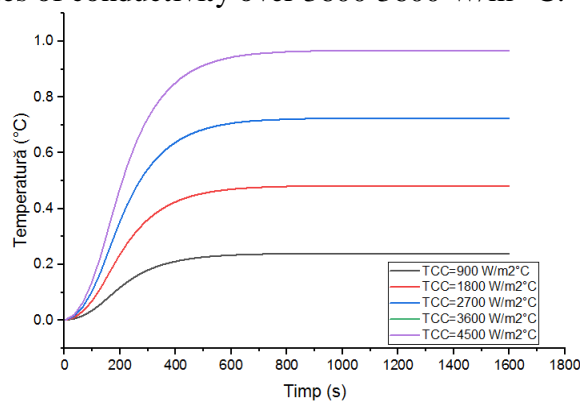
Fig. 4.10. The variation of the temperature with thermal conductivity

Similarly, in the case of the thermal capacitance (noted with C_{th}), the value of $1\cdot10^4$ J/°C satisfies the necessary delay of the system (Fig. 4.11).
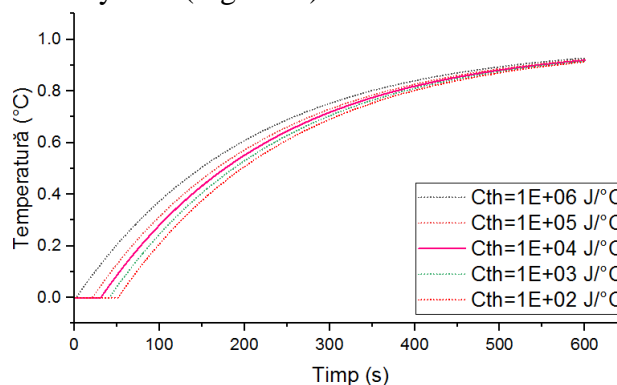
Fig. 4.11. Variation of the system's temperature in time with thermal capacitance

Thus, the correction factors presented in table 4.15 are multiplied by 3600 for K, and those in table 4.16 with $1\cdot10^4$ for τ. These are then transposed into the simulation environment to compensate the model's errors for any studied case.

4.6. Verification of the new proposed simulation model

The verification of the proposed approach is initially carried out by considering the set 3 of plates.

Figure 4.12 illustrates the temperature curves measured with the pyrometer alongside those obtained by FEM simulation (transient thermal analysis) after conductivity and capacitance corrections in the finite element model for plate 11 of set 3.
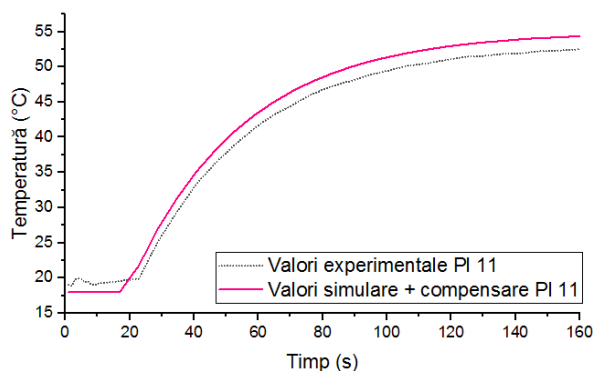
Fig. 4.12. The variation of temperature with time for plate 11. Experimental vs. FEA

Figure 4.13 shows the experimental temperature curves alongside those obtained after conductivity and capacitance corrections in the simulation model for plate 10 from set 3.
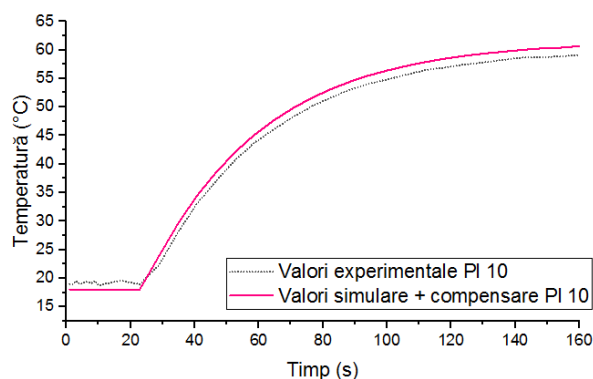
Fig. 4.13. The variation of temperature with time for plate 10. Experimental vs. FEA

The dynamic system characteristics are presented in Table 4.7.

Table 4.7 Dynamic system characteristics for set 3 – Plate 10 and Plate 11

Characteristic	Pl 11			Pl 10		
	Experiments	Simulations	Δ [%]	Experiments	Simulations	Δ [%]
Peak [°C]	59,24	56,77	4,17	55,15	54,23	1,66
Rise time [s]	105,90	103,54	2,22	105,24	101,92	3,15
Settling Time [s]	188,56	184,30		187,39	181,49	

It was observed that the peak temperature error has decreased to a maximum value of 1.66%, while in the case of the rise time and the stabilization time, an error of 3.15% can be observed.

The obtained results demonstrate the accuracy of the model for the five studied plates. However, the verification of the degree of generalization of the model can only be done by extending the study for the set 4 of plates, which was not taken into account when creating the simulation model.

Figure 4.14 presents the results obtained for set 4 plate 13.
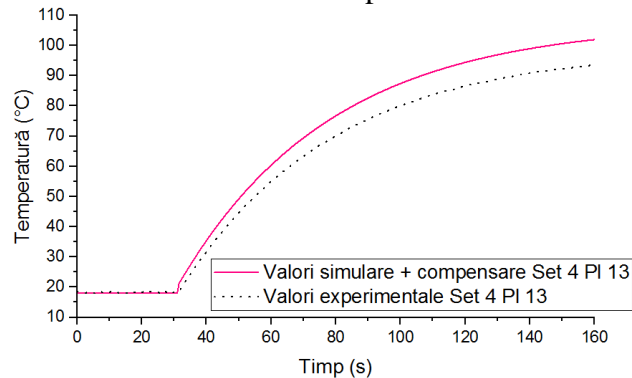
Fig. 4.14. Variation of temperature with time for plate 13. Experimental vs. FEA

Figure 4.15 represents the results obtained for set 4 Plate 12.
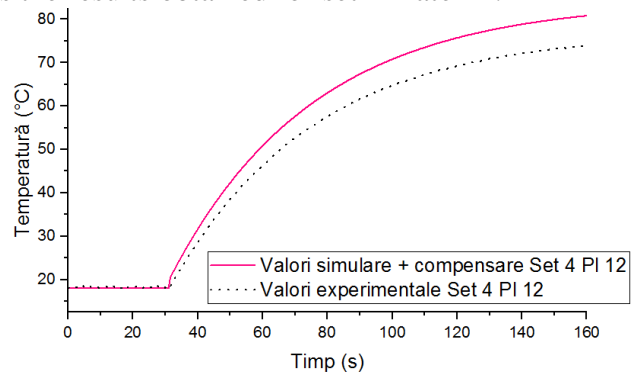
Fig. 4.15. Variation of temperature with time for plate 12. Experimental vs. FEA

In both cases, a difference was observed between the experimental data and the temperatures obtained by simulation. The dynamic system characteristics are compared in Table 4.8.

Table 4.8 Dynamic system characteristics for set 4 – Plate 12 and Plate 13

Characteristic	Pl 12			Pl 13		
	Experiments	Simulations	Δ [%]	Experiments	Simulations	Δ [%]
Peak [°C]	59,00	53,03	10,12	80,70	72,22	10,50
Rise time [s]	96,94	89,46	7,72	106,27	98,46	7,35
Settling Time [s]	172,62	159,29		189,23	175,32	

In this case, the peak temperature error was 10.50%. On the other hand, the rise time and stabilization time error was 7.35%.

Similar errors were observed for plates 12 and 13 from the same set. The results indicate that the approach can be used to make predictions about heat transfer for cases that have not been initially studied. However, it is necessary to both expand the research to increase the generalization degree of the model and to reduce the errors. These aspects are analyzed in Chapter 5 of the Doctoral Thesis.

4.7. Conclusion

The aim of this chapter was to study the influence of gas flow variation on heat transfer in robotic material deposition welding.

The generalization of the model was also checked for set 4. In this case, the peak temperature error was 10.50%. On the other hand, the rise time and stabilization time error was 7.35%. The errors were obviously reduced compared to the initial ones. However, it is necessary to both expand the research to increase the generalization degree of the model and to reduce the errors. These objectives were analyzed in Chapter 5 of the PhD Thesis.

The results confirmed that the simulation model can be used both for the studied plates, but also for anticipating the thermal transfer in robotic material deposition welding for other plates and welding regimes.

Chapter 5. The influence of the gas flow rate on the macro and microstructure of the welded samples at robotic material deposition welding

5.1. Introduction

The purpose of this chapter was to perform visual and profile analyses of cross-section welds, in order to highlight the effects of welding regime parameters on the geometric configuration of the deposited material.

The individual and combined effects of the protective gas flow rate and the inclination angle of the robotic welding gun relative to the weld axis were investigated. Six welding regimes were considered, with the robotic gun positioned perpendicular to the welding surface. For the same regimes, the robotic gun was inclined at an angle of 15° from the normal to the surface of the welded materials.

Within the macroscopic analysis, a visual inspection and measurements with the electronic caliper were performed on 26 plates. The parameters followed in this analysis included: the number of droplets, slag crusts, geometric irregularities, marginal crater, solid film deposits, bead width and bead height.

For the microscopic analysis, samples were taken from eight sets using a cutting machine, from the same area of the plates. The inspected surfaces were sanded on a special machine, chemically treated and cleaned. The parameters inspected in the microscopic analysis were: the ZIT dimensions at the surface of the bead and at its root, the appearance of the weld and the joining angle.

Attention was paid to the calculation of two essential parameters: dilution and cross-sectional area of the weld beads. In the final part of the chapter, the variation of the response size was correlated with the microstructure and macrostructure of the studied samples.

The results of the defectoscopic study were used for the development of a multiple linear regression model. It takes into account independent variables that exhibit a linear relationship with the correction coefficients of conductivity and capacitance identified in Chapter 4 of the PhD Thesis.

A schematic presentation of the research steps and the objectives of this chapter is illustrated in Figure 5.1.
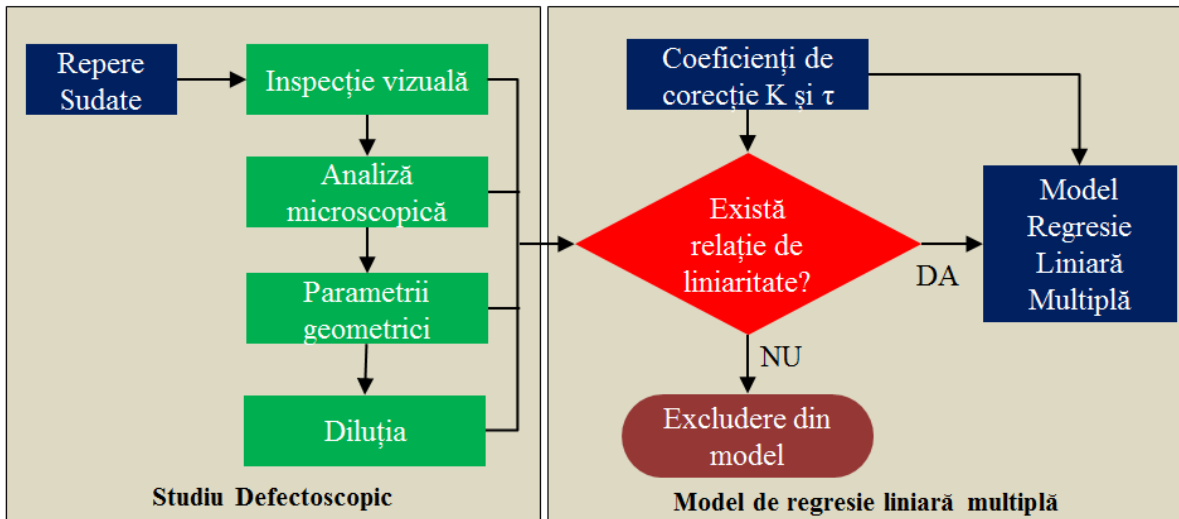
Fig. 5.1. The research steps in Chapter 5

The purpose of this chapter is to solve the objective 5 of the PhD thesis

- **OBJECTIVE 5: Correlation of the response size variation with the micro and macrostructure of the studied samples –** The way in which heat transfer takes place during robotic material deposition welding directly influences the micro and macro structure of the base material. In this sense, defectoscopic studies offer an important perspective on the relationship between welding regime parameters, heat transfer and weld quality. The output is represented by the temperatures measured with the pyrometer.

5.2. Visual analysis of the weld bead

Macroscopic analysis of the samples made by robotic material deposition welding involves a visual inspection, immediately after the material depositions are ready to be taken off the modular table, without any intervention. The defects followed in this subchapter are those in Table 5.1.

Table 5.1 Types of defects observed during the visual inspection

Name, Location
NS – Number of droplets (on the weld bead, on the heat affected zone, at the weld ends, on the base material not affected by heat);
CZ – Slag crusts (small, adherent and glassy films positioned on the weld bead or on the bonding areas with the base material);
NG – Geometric irregularities of the weld bead (thinning, thickening, height reduction, excessive overtopping, solidification scales, etc.);
CM - Marginal crater (solidification crater type crack) usually formed at the weld termination areas, as a result of solidification contraction);

Solid film deposits resulting from oxidation/burning of chemical elements;
B – Weld bead width - Measured with an electronic caliper in the same position on the plate;
h – Weld bead height - Measured with an electronic caliper in the same position on the plate;

Visual inspections and measurements were performed on 8 plate sets. The third set contains 5 plates with gas flow rates of 10 l/min, 13.5 l/min, 17 l/min, 20.5 l/min, and 24 l/min, while the other sets are composed of 3 plates, each with a different welding regime. Details of the welding regime parameters used in the experimental program can be found in Table 5.2 and Table 5.3.

Table 5.2 Welding regime parameters for sets 1-4

The robotic gun is perpendicular to the surface of the plate									
SET	Plate	Type of arc	Gas flow rate [l/min]	Current intensity [A]	Voltage [V]	Welding speed [cm/min]	Electrode diameter [mm]	Feed rate [m/min]	Standoff distance [mm]
1	1	Short arc	10	160	17,7	45	1,2	3.9	15
	2		17						
	3		24						
2	4	Spray arc	10	280	29,2	55	1,2	9	15
	5		17						
	6		24						
3	7	Short arc	10	190	18.9	45	1,2	4,7	15
	8		13,5						
	9		17						
	10		20,5						
	11		24						
4	12	Spray arc	10	320	31,7	55	1,2	11	15
	13		17						
	14		24						

Table 5.3 Welding regime parameters for sets 5-8

The robotic gun is inclined by 15 ° from the normal to the surface of the plate with a pull to the right									
SET	Plate	Type of arc	Gas flow rate [l/min]	Current intensity [A]	Voltage [V]	Welding speed [cm/min]	Electrode diameter [mm]	Feed rate [m/min]	Standoff distance [mm]
5	15	Short arc	10	160	17,7	45	1,2	3,9	15
	16		17						
	17		24						
6	18	Spray arc	10	280	29,2	55	1,2	9	15
	19		17						
	20		24						
7	21	Short arc	10	190	18,9	45	1,2	4,7	15
	22		17						
	23		24						
8	24	Spray arc	10	320	31,7	55	1,2	11	15
	25		17						
	26		24						

In order to ensure a more precise correlation between the employed regime and the description of the defects observed on the plate, the relevant information has been centralized in Table 5.4. The types of defects followed were considered according to SR EN ISO 6520-1:2009 standard. This refers to electric welding and welding processes, providing standardized terms and definitions used in the field of welding, with the aim of ensuring a common and clear understanding of the terminology used [187].

The following parameters are of interest for the macroscopic inspection:

1. **Number of droplets**
2. **Slag crust**
3. **Geometric irregularities**
4. **Solid film deposits**

Table 5.4 Visual analysis of welding defects in 8 sets

PL No.	Welding parameters	Weld analysis According SR EN ISO 6520-1:2009
1	SHORT ARC Torch perpendicular d_g=10 l/min I=160 A U=17,7 V v_s=45 cm/min d_e=1,2 mm v_a=3,9 m/min l_{cl}=15 mm	**B**=5,29 mm **h**=2,45 mm **Number of droplets** – The weld bead has fine droplets on both sides, more pronounced at the end, with larger isolated droplets, but in small number; **Slag crust** - The slag crust is present on the surface of the weld bead in the form of brown films of different sizes and quite pronounced, on both sides of the joining area. **Geometric irregularities** - The weld bead has geometric irregularities only at the beginning and at the end. At the beginning, the height h is higher, and towards the end it decreases. **Solid film deposit** - The solid film deposit is under 10% of the plate surface.
13	SPRAY ARC Torch perpendicular d_g=17 l/min I=320 A U=31,7 V v_s=55 cm/min d_e=1,2 mm v_a=11 m/min l_{cl}=15 mm	**B**=9,23 mm ; **h**=3,59 mm; **Number of droplets** - The number of droplets remains the same, but is smaller than at 12; **Slag crust** - The slag crust is more pronounced on the outer surface of the weld bead, and is thinner at the base of the weld bead than at nr 12; **Geometric irregularities** - The weld bead has geometric irregularities only at the beginning and at the end; **Solid film deposit** - The solid film deposit covers about 75% of the plate surface.

PL No.	Welding parameters	Weld analysis According SR EN ISO 6520-1:2009	
26	SHORT ARC Torch tilt 15 degrees by pulling to the right d_g=24 l/min I=160 A U= 17,7 V v_s=45 cm/min d_e=1,2 mm v_a=3,9 m/min l_{cl}=15 mm	**B**=9,87 mm ; **h**=3,35 mm; **Number of droplets** - The number of droplets is lower than on both plates 24 and 25; **Slag crust** - The slag crust is more pronounced than on the previous plates, with the highest level; **Geometric irregularities** - The weld bead has geometric irregularities only at the beginning and at the end; **Solid film deposit** - The solid film deposit covers over 75% of the plate surface.	

The variation tables presented were employed to identify trends, the materialization of influences or correlations between parameters. They highlight the impact of one factor on others, or on the final result.

In the specific context of weld analysis, a synthetic variation table was created to highlight how different parameters or variables, such as the welding regime, the protection gas flow rate or the welding gun inclination angle affect the geometric parameters, defects or other characteristics of the welds (Table 5.5).

Table 5.5 Variation table for the visual inspection parameters of all sets

Set No.	Number of droplets	Slag crust	Geometric irregularities	Solid film deposit	Weld bead width	Weld bead height
1	↘	↗	—	↗	↗	↗
2	↘	↗	—	↗	↗	↗
3	↘	↗	—	↗	↗	↗
4	↘	↗	—	↗	↗	↗
5	↘	↗	—	↗	↗	↗
6	↘	↗	—	↗	↗	↗
7	↘	↗	—	↗	↗	↗
	↘	↗	—	↗	↗	↗

After the macroscopic analysis of the 26 samples, the following observations can be summarized:

According to Table 5.12, the variation of the gas flow rate affects the width, height, number of droplets, slag crusts, and geometric irregularities of the weld bead as follows:

1. Weld bead width B: The width of the weld bead increased with the increase in gas flow rate.

2. Weld bead height h: At low current intensities, a slight increase in the height of the weld bead was observed with the increase in gas flow rate, but this increase was significant at higher welding current intensities.

3. Number of droplets: The number of droplets was higher for technological regimes in which the gas flow rate was low. This suggests that there is a greater arc stability at higher gas flow rates.

4. Slag crust: The slag crust appears on the surface of the weld bead and in the joining area between the weld bead and the base material:

- The number of films on the surface of the weld bead is proportional to the increase in gas flow rate, and the crust that is formed in the joining area becomes thinner with its increase.

- At an angle of 15° inclination of the robotic torch at high current intensities and high flow rates, the films on the weld bead tend to flow towards the joining area and thus create a large area crust on the lateral surfaces of it.

5. Geometric irregularities: The geometric irregularities are approximately the same at the beginning and at the end of the weld bead, where a difference in height/width can be observed from the rest of the weld bead. At the beginning, the h/B ratio is higher than in the rest of the weld bead, and at the end, the h/B ratio is lower than in the rest of the weld bead. In addition, the smoothness of the weld bead (lack of solidification scale) is lower than in the case of short arc with the torch perpendicular to the surface of the plate.

6. Solid film deposit: The solid film deposit increases at high gas flow rates:
- The solid film deposit is most often distributed symmetrically on both sides of the weld bead.
- Is asymmetric in relation to the length of the plate.
- Is more distinct in the direction opposite the direction of movement of the torch.

5.3. Microscopic analysis of welds in cross section

This subsection aims to compare the microscopic structure of the surface of the samples. The defects presented in Table 5.6 were studied.

Table 5.6 Types of defects monitored during the microscopic analysis

Name and location
ZIT on the surface of the plate
ZIT at the root of the weld
Appearance of the weld
Welding angle

The geometric elements of the type of weld analyzed in the experimental program are presented in Figure 5.2. (According to SR-EN 5817:2003) [188];.
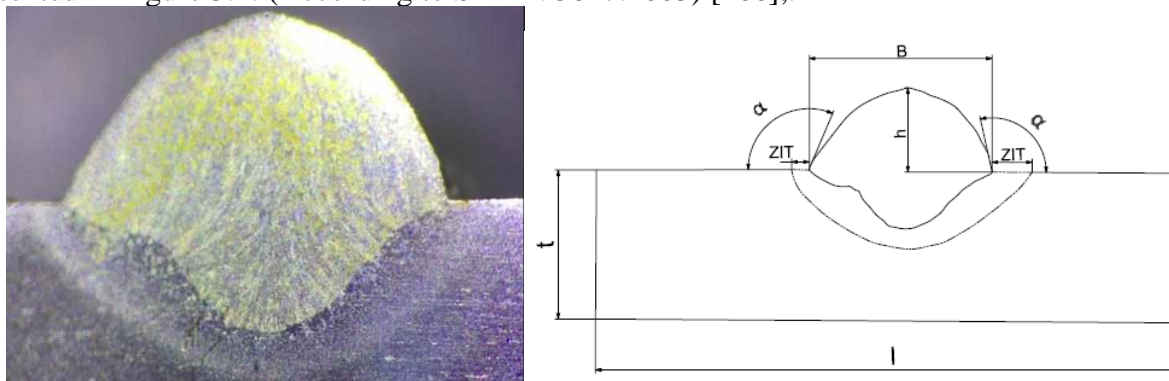
Fig. 5.2 Elements of the welded joint

The symbols in Figure 5.2 are: B - width of the weld bead ; t - thickness of the base material (plate); l - width of the plate; h - height (rise) of the weld bead; α - welding angle ; ZIT - heat-affected zone.

As in the case of the macroscopic analysis, for each of the 8 sets the majority of the welding parameters were kept constant, except the flow rate of the shielding gas.

Table 5.7 Microstructural analysis of set 1

Microstructure image	
Welding angle measurement	**ZIT on the surface of the weld bead**
Appearance of the weld	**ZIT at the root of the weld**
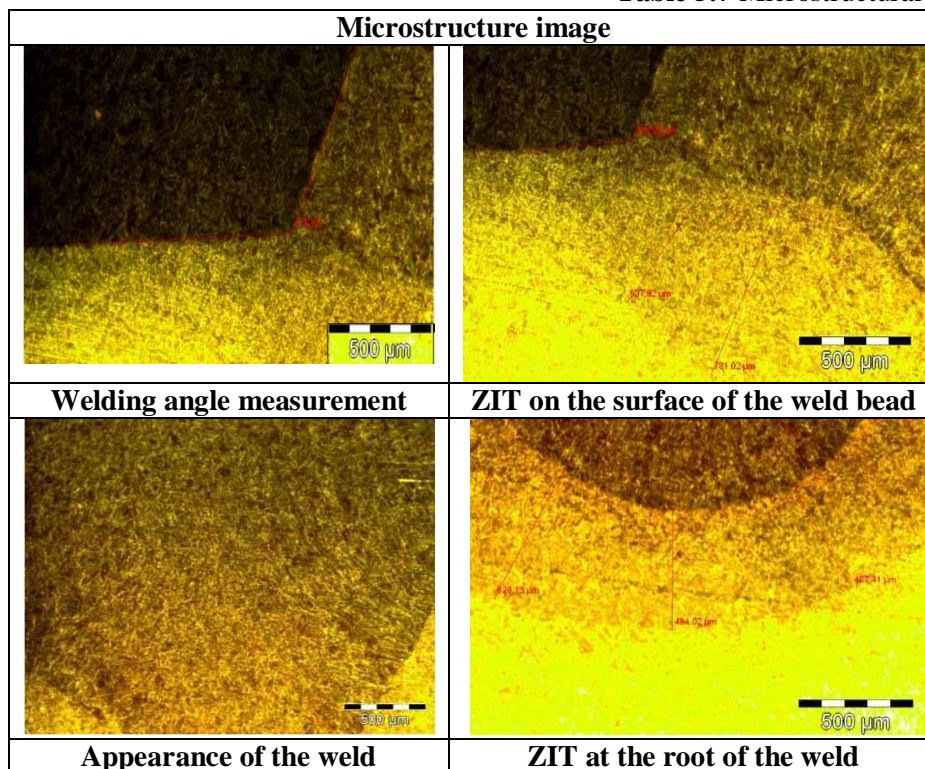
Table 5.8 presents the measured values of the welding angle.

Table 5.8 Welding angle values

Set No.	Welding angle measurement						
1	Plate 1	115,62°		Plate 2	124,78°	Plate 3	122,16°
2	Plate 4	115,20°		Plate 5	104,47°	Plate 6	120,85°
3	Plate 7	92,64°	Plate 8 98,91°	Plate 9 105,19°	Plate 10 105,78°	Plate 11	106,38°
4	Plate 12	122,96°		Plate 13	129,64°	Plate 14	120,05°
5	Plate 15	101,14°		Plate 16	98,78°	Plate 17	126,78°
6	Placa 18	99,78°		Plate 19	105,57°	Plate 20	58,63°
7	Plate 21	115,55°		Plate 22	114,15°	Plate 23	104,25°
8	Plate 24	114,72°		Plate 25	90,50°	Plate 26	104,30°

The measured values of the welding angle for 8 plate sets are presented in Table 5.8.
The following aspects can be highlighted based on the measurements:
- For Set 1, the values are arranged in a concave graph of a quadratic function.
- For Set 2, the values are arranged in a convex graph of a quadratic function.
- For Set 3, the values follow an increasing trend with the increase in gas flow rate.
- For Set 4, the values follow a concave parabola of a quadratic function.
- For Set 5, the values do not follow any trend.
- For Set 6, the values do not follow any trend

- For Set 7, the values follow a decreasing trend with the increase in gas flow rate.
- For Set 8, the values are arranged in a convex graph of a quadratic function.

Table 5.9 Surface ZIT values

Set No.	Surface ZIT extension				
1	Plate 1 478,03 μm		Plate 2 454,44 μm		Plate 3 360,19 μm
2	Plate 4 680,19 μm		Plate 5 757,62 μm		Plate 6 676,67 μm
3	Plate 7 621,04 μm	Plate 8 608,17 μm	Plate 9 601,25 μm	Plate 10 600,26 μm	Plate 11 605,22 μm
4	Plate 12 766,38 μm		Plate 13 631,27 μm		Plate 14 926,22 μm
5	Plate 15 604,16 μm		Plate 16 720,14 μm		Plate 17 750,02 μm
6	Plate 18 594,01 μm		Plate 19 1056,09 μm		Plate 20 984,10 μm
7	Plate 21 665,88 μm		Plate 22 546,87 μm		Plate 23 860,67 μm
8	Plate 24 764,26 μm		Plate 25 750,13 μm		Plate 26 677,20 μm

Table 5.9 summarizes the measured values of the surface ZIT. The following remarks can be done:

- For Set 1, the values decrease as the gas flow rate increases.
- For Set 2, the values are arranged approximately according to the parabola of a concave quadratic function.
- For Set 3, the ZIT fluctuates approximately according to a convex parabola.
- For Set 4, the thermal ZIT is most strongly affected, as this is the case when the shielding gas flow rate is 24 l/min (the largest of the considered ones).
- For Set 5, the diagram reflects the direct proportionality between ZIT and gas flow rate.
- For Set 6, the values are arranged approximately according to the parabola of a concave quadratic function.
- For Set 7, the values are arranged according to a convex graph of a quadratic function.
- For Set 8, the values follow a decreasing trend as the gas flow rate increases.

Table 5.10 Root ZIT values

Set No.	Root ZIT extension				
1	Plate 1 494,02 μm		Plate 2 552,27 μm		Plate 3 690,14 μm
2	Plate 4 490 μm		Plate 5 536,01 μm		Plate 6 596,08 μm
3	Plate 7 490 μm	Plate 8 513 μm	Plate 9 536,01 μm	Plate 10 566,04 μm	Plate 11 596,08 μm
4	Plate 12 534,03 μm		Plate 13 590 μm		Plate 14 466,11 μm
5	Plate 15 596,08 μm		Plate 16 640,31μm		Plate 17 534,03μm
6	Plate 18 796,36 μm		Plate 19 756,86 μm		Plate 20 680,19μm
7	Plate 21 530,54 μm		Plate 22 754,27 μm		Plate 23 620,16 μm
8	Plate 24 570 μm		Plate 25 490 μm		Plate 26 678 μm

Table 5.10 presents the measured values of the root ZIT of plates. The following observations can be done based on it:

- For Set 1, the values increase as the gas flow rate increases. The thermally affected zone at the root increases as the gas flow rate increases.

- For Set 2, the values are arranged approximately according to the parabola of a concave quadratic function.
- For Set 3, the diagram shows an increasing trend, proportional to the higher gas flow rates.
- For Set 4, the values are arranged approximately according to the parabola of a concave quadratic function.
- For Set 5, the values are arranged approximately according to the parabola of a concave quadratic function.
- For Set 6, the root ZIT has different values, but also a clear decreasing trend as the gas flow rate increases.
- For Set 7, the values are arranged approximately according to the parabola of a concave quadratic function.
- For Set 8, the values are arranged approximately according to the parabola of a convex quadratic function.

5.4. Dilution and weld area in section for each welding regime

Dilution is the change in the chemical composition of the filler material caused by mixing with the base material. It is measured as a percentage, and the calculation relationship is:

$$Dilutia = \frac{B}{A+B} \cdot 100 \, [\%] \tag{5.1}$$

Where: B represents the area of the molten metal pool; A represents the area of the filler material (Fig. 5.3).
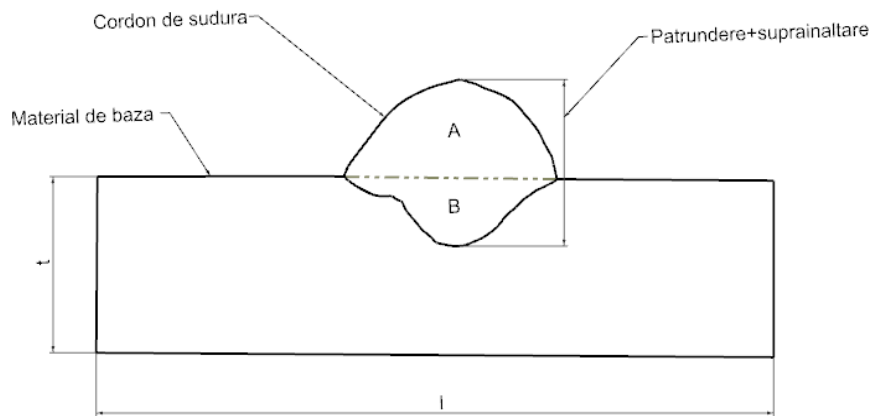
Fig. 5.3 A - area of the filler material; B - area of the molten metal pool; t - plate thickness; l - plate width

Weld area in section A_s:

$$A_s = A + B \tag{5.2}$$

However, a more practical approach can be used, which involves the following steps: • One image was acquired for each sample from the microscope; • The photograph was loaded into NX1980 software; • It was opened in the SCKETCH module; • The weld profile was created; • A partial 3D model of the weld was created and scaled to the real size of the weld; • The total area of the weld was measured;

The values of the measurements and calculations of the parameters are integrated in Table 5.11: cumulative dimensional values of penetration and elevation, the elevation area (A), the penetration area (B), the area for the total cross-sectional area of the weld (As) and dilution.

Table 5.11 Values of dilutions and plate areas

Plate No.	Penetration + Elevation [mm]	As [mm²]	A [mm²]	B [mm²]	Dilution [%]
1	4,37	15,4518	10,4704	4,9814	67,76168
2	4,41	16,8013	11,0527	5,7486	65,78479
3	3,93	14,0144	9,2133	4,8011	65,74167
4	5,90	35,0081	16,3516	18,6565	46,70805
5	6,01	33,3241	16,0058	17,3183	48,0307
6	6,31	38,2751	19,4855	18,7896	50,90908
7	4,74	19,1831	12,8105	6,3726	66,78013
8	4,76	18,99385	12,169	6,82485	64,06811
9	4,78	18,8046	11,5275	7,2771	61,30149
10	4,785	18,06865	11,4421	6,62655	63,32571
11	4,79	17,3327	11,3567	5,9760	65,52182
12	7,61	47,7519	22,8958	24,8561	47,94741
13	7,63	50,2379	22,8958	27,8817	45,09044
14	7,86	50,0451	22,6423	27,4028	45,24379
15	4,08	14,8539	9,664	5,1899	65,06035
16	4,49	15,5962	10,2601	5,3361	65,7859
17	4,55	12,4482	7,9518	4,4964	63,87912
18	6,50	37,4919	19,7107	17,7812	52,57322
19	6,60	39,3019	20,665	18,6369	52,58016
20	6,69	39,1873	21,2933	17,8940	54,33725
21	4,50	15,8143	10,2133	5,6010	64,58269
22	4,61	16,8595	11,3099	5,5496	67,08325
23	4,67	19,2171	13,0287	6,1884	67,79743
24	7,52	45,1558	23,361	21,7948	51,73422
25	7,58	48,1566	24,4476	23,7090	50,76687
26	7,64	44,5402	22,9449	21,5953	51,51504

The trends in the variation of microscopic characteristics have been centralized in Table 5.12 for the evaluation of the linearity trends between values. It was observed that these trends were attained in the case of penetration and overshoot, fillet angle, root ZIT and dilution.

Table 5.12 Table of the geometric parameters variation, microscopic defects and dilution

Set No.	Plates	Penetration and Elevation	Welding angle	ZIT on the surface of the plate	ZIT at the root of the weld	Weld area in section	Dilution
1	1-2	↗	↗	↘	↗	↗	↘
	2-3	↘	↘	↘	↗	↘	↘
2	4-5	↗	↘	↗	↗	↗	↗
	5-6	↗	↗	↘	↗	↘	↗
3	7-8	↗	↗	↗	↗	↗	↘
	8-9	↗	↗	↗	↗	↗	↘
	9-10	↗	↗	↗	↗	↘	↗
	10-11	↗	↗	↗	↗	↘	↗
4	12-13	↗	↗	↘	↗	↗	↘

Set No.	Plates	Penetration and Elevation	Welding angle	ZIT on the surface of the plate	ZIT at the root of the weld	Weld area in section	Dilution
	13-14	↗	↘	↗	↘	↘	↗
5	15-16	↗	↘	↗	↗	↗	↗
	16-17	↗	↗	↗	↘	↘	↘
6	18-19	↗	↗	↗	↘	↗	↗
	19-20	↗	↘	↘	↘	↘	↗
7	21-22	↗	↘	↘	↗	↗	↗
	22-23	↗	↘	↗	↘	↗	↗
8	24-25	↗	↘	↘	↘	↗	↘
	25-26	↗	↗	↘	↗	↘	↗

5.5. Correlation of the geometric parameters, microstructural defects and dilution with correction coefficients of the dynamic system

Table 5.12 shows that the gas flow rate has a significant influence on the microstructure of the welds obtained by robotic welding. On the other hand, the gas flow rate directly influences the heat transfer of the process. In this sense, the correction coefficients applied to the first-order system make the transition from the perfect thermal conductivity to the real behavior of the technological process.

Multiple linear regression

In Figure 5.4, the trend between the correction coefficient C_K and the experimentally measured dilution (a), together with the correction coefficient C_T and dilution (b) can be observed.

a   b
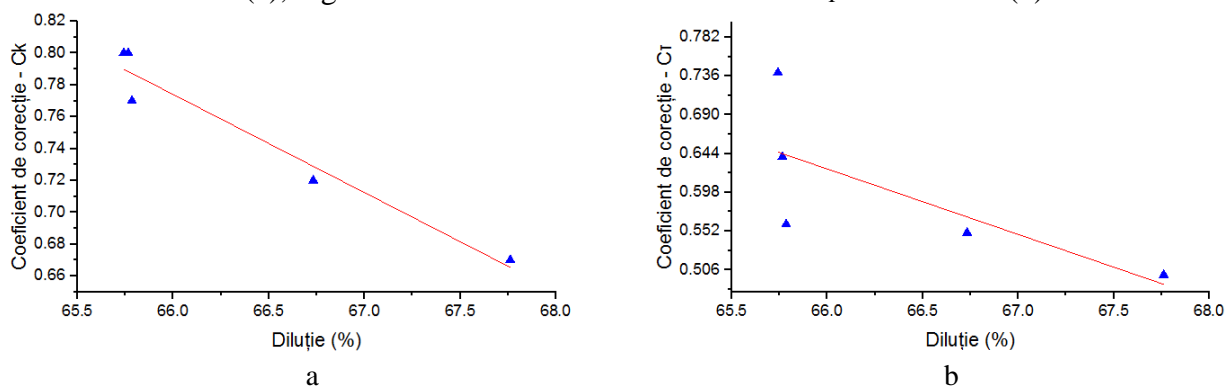
Fig. 5.4 Linear variation of the correction coefficients – K (a) şi τ (b)

Therefore, a multiple linear regression study can be conducted to correlate the K and τ corrections with the geometric parameters, microstructural defects, and dilution resulting from the study. Thus, the following dependent variables will be taken into account: • Geometry: penetration + weld bead rise, weld bead cross-sectional area; • Microstructural defects: fillet angle, ZIT at the plate surface, ZIT at the weld bead root; • Dilution; The independent variables are represented by the K and τ correction coefficients. Table 5.13 summarizes the values that were included in the simulation study.

Table 5.13 Dependent and independent values

		Dependent values			Independent values	
d_g [l/min]	Dilution [%]	Penetration + Elevation [mm]	Root ZIT values [µm]	Welding angle [º]	C_K	C_τ
10	66,78	4,74	490	92,64	0,67	0,5
13.5	64,06	4,76	513	98,91	0,72	0,55
17	61,30	4,78	536	105,19	0,77	0,56
20.5	63,32	4,785	566	105,78	0,8	0,64
24	65,52	4,79	596	106,38	0,8	0,74

In the second step, the identification of the β coefficients is performed using the bisection method implemented in Microsoft Excel – Regression add-in Toolpack. The parameters of set 3 are employed to define the model.

Table 5.14 shows the errors obtained in the prediction of the K and τ correction coefficients..

Table 5.14 Regression statistics

Plate	C_K errors			C_τ errors		
	Actual C_K	Estimated C_K	ε (%)	Actual C_τ	Estimated C_τ	ε (%)
1	0,67	0,65	3,25	0,5	0,49	2,56
2	0,72	0,70	2,63	0,55	0,52	6,42
3	0,77	0,75	2,14	0,56	0,54	2,69
4	0,8	0,77	3,99	0,64	0,63	1,99
5	0,8	0,78	1,96	0,74	0,72	3,22

It can be observed that the maximum error for estimating the correction coefficients is 3.99% in the case of C_K and 6.42% in the case of C_τ, which confirms a good prediction. Table 5.15 shows the values of the β constants obtained as a result of the study.

Table 5.15 β coefficients

Coefficient	Significance	Value for C_K	Value for C_τ
β_0	Intercept	-0,23	-2,69
β_1	d_g	0,01	0,01
β_2	Dilution [%]	0,01	0,03
β_3	Penetration + Elevation [mm]	-0,08	0,04
β_4	Root ZIT values	0,00	0,00
β_5	Welding angle	0,01	0,01

Verification of the methodology for set 4

The verification of the generalization degree of the methodology can only be achieved by extending the study to a set of plates that were not included in the initial data set. Therefore, set 4 is taken into account.

Table 5.16 shows the values included in the regression model. The β constants from table 5.26 were considered for making predictions of the independent values.

Table 5.16 Dependent and included values in the study for set 4

|		Dependent values		
d_g [l/min]	Dilution [%]	Penetration + Elevation [mm]	Root ZIT values [μm]	Welding angle [º]
10	47,94	7,61	534,03	122,96
17	45,09	7,63	590	129,64
24	45,24	7,86	466,11	120,05

Table 5.17 shows the predicted values of the constants K and θ. It can be observed that they differ from the values obtained in the previous chapter.

Table 5.17 Predicted values of the correction constants K and θ for set 4

d_g [l/min]	Predicted values set 4		Initial values set 4	
	C_k	C_τ	C_k	C_τ
10,00	0,60	0,46	0,67	0,50
17,00	0,64	0,51	0,77	0,56
24,00	0,70	0,52	0,80	0,74

The new constants were included in the simulation model.

Figure 5.5 and 5.6 show a comparison between the results obtained using the two simulation models: one based on the simulation model from the previous chapter and the other that includes the correction constants anticipated by the regression model. By analyzing these figures, the impact of adding the correction constants on the accuracy and validity of the simulation model can be evaluated, thus providing important information for the development and improvement of the regression model in the specific context of the study.
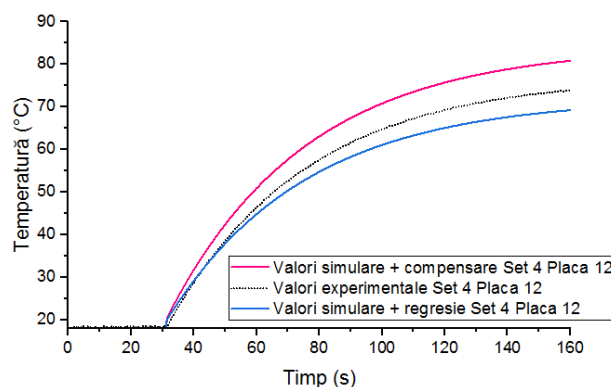
Fig. 5.5 Temperature variation over time for set 4 – Plate 12 considering experimental values, simulation with compensation and the regression model
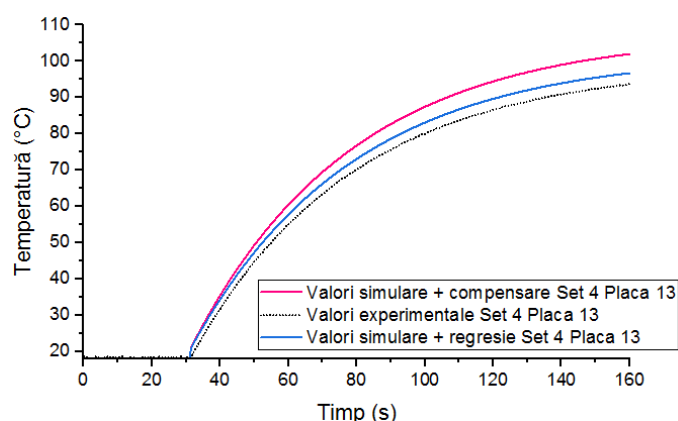
Fig. 5.6 Temperature variation over time for set 4 – Plate 13 considering experimental values, simulation with compensation and the regression model

The dynamic system characteristics are presented in tables 5.18 and 5.19 for set 4.

Table 5.18 Dynamic system characteristics for set 4 Plate 12 and Plate 13

Characteristic	Set 4 Plate 12			Set 4 Plate 13		
	Experiments	Simulations	Δ (%)	Experiments	Simulations	Δ (%)
Peak (°C)	59,00	57,38	2,75	80,70	78,85	2,29
Rise time (s)	96,94	95,05	1,95	106,27	104,40	1,76
Settling Time (s)	172,62	169,25		189,23	185,90	
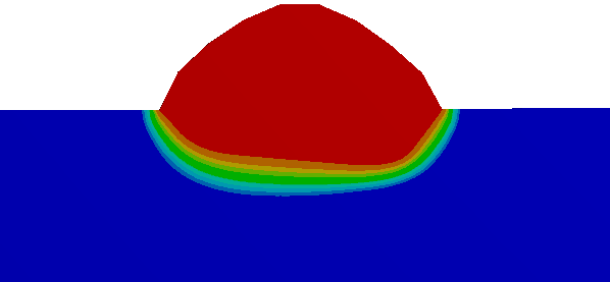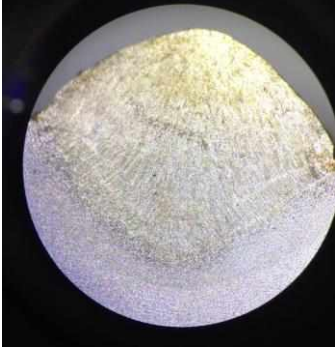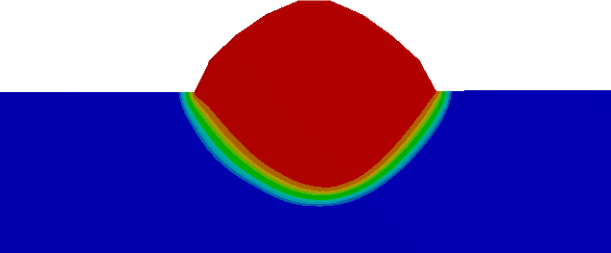
Table 5.19 Dynamic system characteristics for set 4 Plate 14

Characteristic	Set 4 Placa 14		
	Experiments	Simulations	Δ (%)
Peak (°C)	105,70	102,68	2,85
Rise time (s)	103,52	102,21	1,27
Settling Time (s)	184,34	182,00	

The maximum error in the peak temperature is 2.85%. On the other hand, the maximum error in the rise and stabilization time is 1.95%. The values obtained prove that there is a close relationship between the geometric parameters, microstructural defects, dilution and K and τ corrections applied to the simulation model. At the same time, the results demonstrate that the gas flow influences the way the heat transfer is carried out in material deposition by robotic welding. In turn, it governs the appearance of defects at the level of the deposited material. The confirmation of these aspects also requires the processing of the results obtained at the ZIT level, with reference to images captured using an optical microscope.

Table 5.20 shows sections that were cut at the center of the weld bead for set 4 – Plate 12.

Table 5.20 ZIT sections from the simulation model and the microscopic observation for set 4 plate 12

| Simulation section – Base model Δt = 10 s | |
| Simulation section – Model with regression correction Δt = 10 s | ZIT – Observed under a microscope |

Both the initial simulation model and the model that takes into account the corrections applied through regression are taken into account. In both cases, the simulation time chosen is 10 seconds: 8.7 seconds necessary for generating the bead + 1.3 seconds to allow the formation of the gradient. It was observed that in the case of the base model, the temperature gradient is more distinct at the level of the filler material, while a fraction of the gradient is visible at the level of the base material. On the other hand, the interface conductance compensation facilitates heat transfer to the interaction zone between the bodies. Thus, the thermal gradient at the level of the reference follows the same trend as the ZIT observed under the microscope.

The results of the study highlight the correlation between geometric parameters, microstructural defects, dilution and K and τ corrections, both by processing the values on the surface and in the depth of the model.

5.6 Conclusion

The results indicate that the gas flow influences the way the macroscopic defects appear, in the following (according to table 5.5):

- The bead height varies slightly at low current intensities and significantly at higher current intensities.
- The number of droplets is higher at lower flow rates, indicating better arc stability at higher flow rates.
- The number and thickness of slag crust films on the bead vary proportionally with the gas flow rate.
- The geometric irregularities at the beginning and end of the bead are of the same type, but the height/width ratio values are higher at the beginning and lower at the end, these differences being more noticeable especially at the gun tilt.

- Solid film deposits are influenced by the gas flow rate, but no clear trend can be observed.

The results of the Penetration + Elevation graphs indicate a variation of the values proportional to the gas flow rate, with the exception of the first group of three plates (according to table 5.12).

With regard to the graph of the total cross-sectional area of the bead, a direct proportionality trend between the area and the gas flow rate was observed in four out of the eight analyzed sets (according to figure 5.9).

The configuration of the trends for the bead cross-sectional area remains similar to that of the total area in the diagrams for each set individually (according to table 5.12).

By analyzing the variation of the values in the dilution diagram, grouped in three and five plates, the hypothesis is made that they are interdependent with the gas flow rate (according to table 5.12).

The regression model was developed using Microsoft Excel. The maximum error of the algorithm was 6.42% in the case of estimating the τ correction coefficient for plate no. 2 from set 3.

It was observed that the maximum error of the dynamic system characteristics decreased to 2.85% in the case of the peak temperature for set 4 plate 14.

The results attest that there is a close relationship between the parameters, in the deposition of material by robotic welding. Thus, the correction coefficients materialize the deviation from the simulation model in which the interaction between bodies is an ideal one. On the other hand, these coefficients are influenced by the gas flow which in turn influences the shape of the deposited material.

The limitation of the approach is that the generalization of the regression model was performed on two sets of plates with the same torch tilt. In the future, a study is required in which the torch tilt is also considered, since it has been observed from chapters 4 and 5, that the influence of the gas flow variation manifests itself both on the heat transfer and on the macroscopic and microscopic characteristics, regardless of the tilt in the deposition of material by robotic welding.

Chapter 6. Conclusions

6.1 General conclusions

In the current context of industrial engineering, robotic material deposition facilitates the repair or restoration of worn components or parts. This avoids the need to manufacture new parts and implicitly reduces the consumption of raw materials. On the other hand, robotic welding allows for better process control, reducing heat losses and minimizing energy consumption. In addition, by reusing and refurbishing components, the need to produce and transport new parts is avoided, which can lead to savings across the entire supply chain.

However, one disadvantage of the material deposition process by welding is the existence of the **heat-affected zone (ZIT).** This locally modifies the microstructural characteristics of the base material. For this reason, the ZIT has inferior mechanical properties than the base material, and there is a risk of cracks appearing and propagating.

The welding regime parameters in robotic material deposition have a significant impact on the (ZIT) and implicitly on the quality of the weld, mechanical properties, temperature distribution, energy efficiency and cycle time. The scientific literature on this topic comprises recommendations for the optimal welding voltage, current intensity and speed for different materials and technologies.

The variation of the welding regime parameters affects the way in which heat transfer takes place at the base material level. The welding voltage influences the temperature gradient in the ZIT

because it determines the amount of electrical energy transferred to the workpiece. A higher welding voltage will dissipate more heat. On the other hand, the current intensity contributes to heat dissipation due to electrical resistance. There are a multitude of scientific papers that focus on these parameters and on the micro and macro structural influence that act at the level of the deposited material.

Capturing temperature gradients during the welding process involves the use of non-contact measurement techniques. In this sense, **infrared thermography** is the most used instrument because it ensures the acquisition of temperatures in ranges that capture phase changes. At the same time, depending on the specifications of the acquisition system, temperatures at the arc level can also be processed.

A preliminary step in the development of heat transfer simulation models in robotic material deposition **is the three-dimensional representation of the base material and the weld bead**. In the literature, this assembly is mostly represented in an ideal form, neglecting the deviations that occur due to the surface preparation state, the equipment operation mode, or the conditions in the technological environment. From this point of view, 3D surface reconstruction is a technique that can reproduce the real shape of the studied geometry with an accuracy of the order of millimeters. Although 3D scanning techniques for welded parts are presented in the literature, they generally refer to the use of point clouds to serve the non-destructive testing processes.

The simulation of heat transfer in robotic material deposition is studied in a wide range of works. The problem can be described by two major domains: the solid domain, which materializes the base material and the deposited material, and the fluid domain, which represents the interaction between the shielding gas and the welded part. For CFD analysis of heat transfer in electric arc welding, laws such as mass, energy, and impulse conservation, together with Fourier and Newton's laws of heat transfer, are necessary. These facilitate the modeling of the shielding gas flow, the temperature distribution, and the heat transfer that occurs at the weld pool level. On the other hand, the influence of the fluid domain can be approximated and studied based on the forced convection coefficient. This is influenced by the interaction between the shielding gas and the outer surfaces of the part. From this perspective, FEA simulation models can capture the temperature gradient of the robotic material deposition process by solving the heat transfer equations through conduction and convection. Alternatively, CFD and FEA simulations can be correlated to synchronize the boundary conditions in the fluid and solid domains. The literature includes a wide range of research through simulation. However, the generalization of the existing methodologies cannot be achieved because each study describes a case that is validated through a customized experimental stand, new perspectives being always needed.

The shielding gas flow rate in robotic material deposition affects heat transfer because the turbulent flow regime of the latter directly influences the heat exchange between the weld bead and the environment through forced convection. On the other hand, the pressure exerted on the melted metal column modifies the conductivity at the junction between the base material and the deposited material. Although the simulation models presented in the literature have the flexibility to modify the parameters of the welding regime, there are no works in which the effect of the shielding gas on heat transfer at the level of the welded part is studied. On the other hand, the results of experimental research are usually employed only to verify the results of the simulation models, and there is no two-way synchronization between the simulation and the experimental procedures.

Any change in the welding regime has a direct impact on heat transfer. On the other hand, **heat transfer influences the micro and macrostructure of the welded parts**. From this point of view, the correlation between the results of the heat transfer analysis and the defectoscopy study of samples creates a starting point for understanding the relationship between the two phenomena. In this sense, the visual inspection of the number of droplets, approximation of the slag crust dimensions and the bead irregularities are essential steps in a macroscopic study. On the other hand, the dimensions of the heat-affected zone (ZIT) at the surface and root of the bead, the appearance of

the weld, the joining angle and the dilution provide the information necessary for the microscopic study.

The scientific relevance of the subject can be associated with the European Energy Efficiency Directive (2012/27/EU). This directive aims to adopt more efficient practices and technologies to reduce energy consumption and, implicitly, the associated raw materials. By correlating the thermal phenomena of the deposition process with the micro and macrostructural phenomena, useful conclusions were drawn regarding the optimal parameters of the gas flow rate that ensure a balance between its consumption, temperature gradients and the quality of the weld.

The results of this research have a potential impact on robotic welding by proposing technological recommendations to improve the process. On the other hand, the correlation between experimental and simulation methodologies and the optimization of the information flow between the two environments allowed the extension of the proposed approach for any set of parameters and any type of part or welding technology. Also, from a methodological point of view, CFD-FEM simulations have been successively improved by introducing experimental data in the simulation models.

Research methodology

Figure 6.1 illustrates the research methodology in an algorithmic form. In addition to the main stages, the intercorrelation and synchronization of the modeling and simulation results with the macro and microscopic studies can be observed.

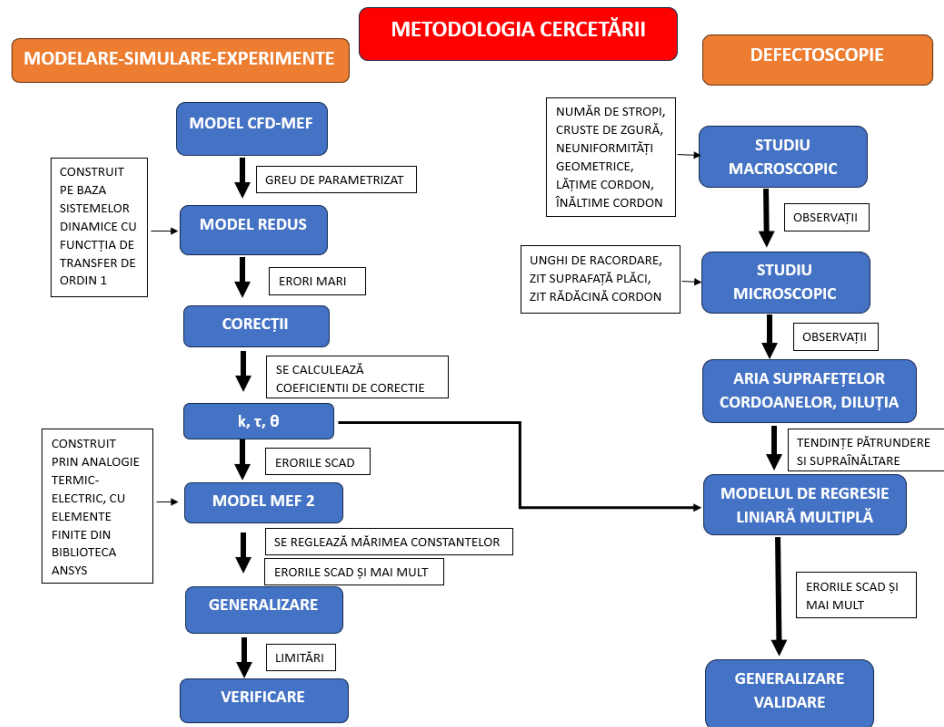**Fig. 6.1** Research methodology

The originality of the Doctoral Thesis is supported by the lack of clear formulations in the literature regarding the influence of gas flow on the heat transfer in robotic material deposition welding. The present work brings 28 original contributions, grouped as follows:

- 12 theoretical contributions
- 5 methodological contributions
- 8 experimental contributions

- 3 major contributions on modeling and simulation

To achieve the main objectives of the thesis, a number of additional specific objectives were identified:

- The design of an experimental stand for the robotic material deposition welding process that includes thermal acquisition devices
- The use of non-contact temperature acquisition systems considering two distinct measurement ranges and two specific equipments
- The design of a CFD simulation model for calculating the forced convection coefficient at the interface between the protective gas and the solid domain
- The development of a FEA simulation model for calculating the temperature distribution using experimental data and the interpolated convection coefficient from the CFD analysis
- The parameterization of the simulation model using transfer functions
- The development of analytical models for identifying the relationship between the variation of the welding regime and the first-order system constants
- Defectoscopic research for the micro and macrostructural analysis of the studied samples.

Chapter 3 aimed to develop an original simulation model of heat transfer in robotic material deposition welding.

In the first stage, experimental research on heat transfer in robotic material deposition welding was carried out. The base material was a S235JR steel plate. It was subjected to the MIG/MAG robotic material deposition process. The chosen shielding gas was a mixture of Argon - Carbon Dioxide (82% Ar 18% CO2). The technological regime parameters were set in accordance with the type and material properties and the robotic welding process. The experimental stand was set on the basis of a robotic welding cell.

The temperature measurement was carried out using two non-contact acquisition systems: a thermal imaging camera with a measurement range of (+500 to +2000 / 2300 °C) and a pyrometer with a measurement range of (-50 °C to +800 °C). The first measurement system captures the temperatures during the welding cycle, while the second performs the measurement in a location outside the ZIT, for the entire welding - cooling sequence. The experimental results were processed in the form of graphs, and were later used for the development and verification of the accuracy of the simulation model.

The real geometry of the welded part was scanned in 3D. Thus, the real shape of the weld bead and the deviations that occur at the base material level were obtained. The geometry reconstruction has been performed by an Reverse Engineering procedure, using ANSYS SpaceClaim and DesignModeler environments.

The development of the simulation model involved two domains of the problem for solving the heat transfer in the robotic material deposition welding: the fluid domain (materialized the interaction between the shielding gas and the welded part) and the solid domain (composed of the base material and the weld bead).

The cooling effect of the shielding gas was captured by CFD analysis. This was performed in the flow domain bounded by walls, a gas inlet zone (torch nozzle) and an outlet zone. Discretization was performed by refining the model in the interaction zones, while the rest of the model was coarsely discretized. The simulation conditions were defined in accordance with the flow rate and the characteristics of the shielding gas. The results were: the fluid velocity vector, the convergence graph of the residuals and the tabular representation of the forced convection coefficient.

The transient thermal FEA analysis aimed to calculate the temperature distribution at the solid domain level. In this case, the discretization was predominantly performed with hexahedras, with a high degree of refinement at the weld bead level and in the interaction zone with the base material. The simulation conditions were defined in accordance with the welding speed and the maximum temperatures that were measured for 27 weld bead segments. The segment activation during the simulation was carried out using the "Birth and Death" technique. The heat exchange between the welded part and the ambient environment was taken into account by defining the forced convection (obtained from the CFD analysis) and the free convection (from the theory of horizontal surfaces). The processed results were: the temperature distribution on the outer faces of the welded deposition elements and in the weld bead section.

The validation of the simulation model was performed by comparing the simulation temperature curve with the one obtained from the experiments. The statistics of the two curves indicated a good fit at the thermal equilibrium (ε=2.11% in the case of the maximum value). Differences of 4.8% between the minimum values appeared due to the noise in the experimental data (visible in the first 15 seconds, because of the electromagnetic interferences generated by the arc ignition, which were not taken into account in the simulation model).

However, it was found that there is an error of 11.08% in the system stabilization time. This can be explained by the fact that the model does not take into account the temperature-dependent material properties (this information is not provided by the manufacturer). Therefore, the correction of the dynamic response can be obtained by adjusting the system capacity.

Although the simulation model was validated for a set of parameters, the research objective was to obtain the generalization of the model, considering different values of the gas flow rates. In the same time, it was important to improve the dynamic response of the simulated system by reducing the error of the stabilization time. These aspects were analyzed in the next chapter.

Chapter 4 aimed to study the influence of gas flow variation on heat transfer in robotic material deposition welding.

Six sets of plates were considered, each set including three metal plates, except the set 3, which included five metal plates. Set 3 was used for the parameterization of the simulation model and for the verification of the results.

For each set, the welding regime was constant, except the gas flow, which had the values of: 10; 13.5; 17; 20.5 and 24 l/min. The experimental procedure was identical to the one presented in the previous chapter, except for the synchronization of the welding cycle times with the data acquisition times.

In this new study the dynamic system characteristics highlighted that the heat transfer is improved in the case of high gas flow values, while the temperatures measured outside the ZIT decrease at low gas flow values (according to paragraph 4.3).

The parameterization of the simulation model involved, in the first step, the delimitation of the weld bead in 27 cross-sections. The geometry can be modified/sampled in this way for any file taken from 3D scans.

A study was carried out to parameterize the gas flow, in which the fluid velocity was gradually increased from 1.08 to 2.16 m/s. It was observed that the flow path was not affected by these changes. On the other hand, the convection coefficient increased with the fluid velocity in all locations of the model. The employment of the polynomial regression has been proposed, to determine the scaling factor of the convection coefficient with respect to the gas flow.

The simulation model was verified for the studied sets. Large discrepancies were observed in the dynamic response of the system, with errors of 28% in the case of peak temperatures and 52.7% in the case of rise and stabilization time. Consequently, the approach could not be used as such.

The theoretical explanation of the errors obtained after the study was performed on the basis of the theory of heat conduction. This is influenced by the pressure exerted by the shielding gas on the weld pool. Thus, a larger fraction of the energy released by the filler metal is transferred to the base material, resulting in higher temperatures outside the ZIT.

The determination of the corrections necessary for the simulation model could be efficiently performed by using first-order delay systems. These were used to model the dynamic response of the studied system, neglecting the equations that govern the heat transfer from the FEA thermal analysis.

The identification of the constants of the single-pole transfer function that govern first-order systems was carried out using the surface method proposed by Nishikawa. The algorithm was implemented in the MATLAB numerical computing environment.

The differences between the gain factors, time constants and delay of the system obtained by comparing the experimental values with those obtained from the simulations determined the correction coefficients. The identification of the relationship between the gas flow and the values of these coefficients allowed the generalization of the model for any given case.

The implementation of the procedure in the simulation environment implied the realization of a sensitivity study (according to Figures 4.20 and 4.21). Its role was to determine the conductivity for which the system temperature no longer varies and the capacitance for which the delay of the dynamic response corresponds to the experimental one.

The verification of the proposed strategy was carried out in a first stage for set 3. In this case, errors of 4.17% were obtained for the peak temperature and 3.15% for the rise and stabilization time.

The degree of generalization was checked for set 4. In this case, the peak temperature error was 10.12%, the rise and stabilization time error were 7.35%. These values were clearly reduced compared to the initial ones. However, it was necessary to both expand the research to increase the degree of generalization of the model and to reduce the errors. These aspects were analyzed in Chapter 5 of the Doctoral Thesis.

The results obtained confirmed the fact that the model can be used successfully for cases that have been included in the model, but also for predicting the heat transfer mode for cases that have not been studied initially.

Chapter 5 primarily examined the non-destructive testing of the markers obtained by material deposition through robotic welding for different welding regimes.

The first part of this study presented the visual inspection of the plates taken from the experimental stand. The parameters of this study were: number of droplets, slag crusts, geometric irregularities of the weld bead, marginal crater, solid film deposits resulting from burning, cross-sectional width of the weld bead and cross-sectional height of the weld bead.

All these defects were centralized in Table 5.4. The analysis and observations were done comparatively on the plates of each set, in order to highlight the influence of the gas flow rate. In total, 8 sets were studied, each set consisting of 3 or 5 plates.

The results indicated that the gas flow rate influences the way in which macroscopic defects appear, in the following ways (according to Table 5.5):
- The height of the weld bead clearly varies with the gas flow rate. This is even more evident at high welding current intensities.
- The number of droplets is higher at lower flow rates, indicating better arc stability at higher flow rates.
- The number and thickness of the slag crust films on the weld bead vary proportional to the gas flow rate.

- The geometric irregularities at the beginning and end of the weld bead are of the same type, but the height-to-width ratio is higher at the beginning and lower at the end, these differences being more noticeable especially at the gun inclination.
- Solid film deposits are influenced by the gas flow rate, but no clear trend can be observed.

In the second part of the study, microscopic features such as the welding angle, the appearance of the weld, and the extension of the heat-affected zone (ZIT) to the surface of the plate and the root of the weld bead were analyzed.

The study of these defects was carried out in the LAMET laboratory (room CK 106) at POLITEHNICA University of Bucharest, using: a high-precision machine for cutting metallographic samples (ISOMET 4000 Buehler), a machine for automatic grinding and polishing of metallographic samples (Vector and Alpha Beta Polisher Buehler).

For the inspection of microscopic defects, samples were taken from the plates obtained by robotic welding deposition using the ISOMET 4000 Buehler machine. Subsequently, the surfaces of these samples were processed on the automatic grinding and polishing machine.

The detection of the defects was done by preparing the surfaces. This process was carried out using a chemical reagent based on Nital (2%).

The defectoscopic process was carried out using the Olympus GX 51 optical microscope. Differences between the compared plates were observed regarding the results of the analyzed features. It was also noticed that at the base of the weld bead, small voids are formed in the case of the use of large gas flow rates, or when the robotic gun is inclined. These voids can be potential locations for the appearance of cracks in the weld.

In the third part of the chapter, the analysis focused on the study of the area of the weld bead surfaces in cross-section and the study of the dilution. For this purpose, images were saved from the microscope using a camera. These were imported into the NX 3D software, being subjected to the scaling process to the real dimensions. The areas of the weld bead surfaces in cross-section were measured on the resulting models. In conclusion, the dilution was determined based on the areas calculated for each cross-section of the weld bead.

The results of the Penetration+Overhead graphs indicated a variation of the these parameters proportional to the gas flow rate, with the exception of the first group of three plates (according to Table 5.12).

Regarding the graph of the total area of the weld bead section, a direct proportionality trend between the area and the gas flow rate was observed in four out of the eight analyzed sets (according to Table 5.12).

The configuration of the trends for the cross-sectional area of the weld bead is maintained similar to that of the total area in the diagrams for each set individually (according to Table 5.12).

By analyzing the variation of the values in the dilution diagram, grouped in three or five plates, it was presumed that they are interdependent with the gas flow rate (according to Table 5.12).

In the last part of the study, a multiple linear regression model was developed in order to correlate the correction coefficients identified in the previous chapter with geometric parameters, microstructural defects and dilution evaluated in this chapter.

In the first stage, the variables that did not represent a linear relationship with the K and τ corrections were removed from the study (according to Table 5.12). These were: ZIT at the surface of the weld bead and the area of the plates. The regression model was developed using Microsoft Excel. The maximum error of the algorithm was 6.42% in the case of the estimation of the τ correction coefficient for plate no. 2 of set 3.

The generalization of the correlation obtained by multiple linear regression was verified for set 4. In this case, the anticipated correction coefficients were included in the simulation model developed in Chapter 4. It was observed that the maximum error of the dynamic system characteristics dropped to 2.85% in the case of the peak temperature for plate 3 of set 4.

The results confirmed that in robotic welding deposition, there is a close relationship between the K and τ correction coefficients with geometric parameters, microstructural defects and dilution. Thus, the correction coefficients materialize the deviation from the simulation model in which the interaction between bodies is an ideal one. On the other hand, these coefficients are influenced by the gas flow rate, which in turn influences the shape of the deposited material.

The limitation of the correlation is that the generalization of the regression model was performed on two sets of plates with the same torch inclination. In the future, a study is needed that takes into account the torch inclination as well, since it was observed from Chapters 4 and 5 that in robotic welding deposition, the influence of the gas flow rate variation manifests itself both on heat transfer and on macroscopic and microscopic characteristics.

6.2 Original contributions of the Doctoral Thesis

The following contributions can be highlighted:

- **Theoretical** contributions:
  1. The use of histograms for filtering the noise produced by the electric arc in the case of infrared thermography of robotic welding processes.
  2. Processing the thermal equilibrium and the stabilization time of the experimental / simulated curves based on the statistical signal processing.
  3. Processing the dynamic characteristics of the thermal curves obtained from experiments and simulations.
  4. Identification of the variation law of the convection coefficient as a function of the gas flow rate from the CFD analysis.
  5. Compensation of the errors of first-order systems by calculating the correction coefficients.
  6. Generalization of the relationship between gas flow rate and correction coefficients.
  7. Comparative study of ZIT both on the surface of the plates and at their root.
  8. Calculation of the dilution, penetration and cross-sectional height of the beads obtained for several welding regimes.
  9. Comparative analysis of the specific joining angles of the studied plates.
  10. Development of a multiple linear regression model for the generalization of the relationship between geometric characteristics, microstructural defects, dilution and correction coefficients k and τ.

- **Experimental** contributions:
  1. Establishment of the technological regime parameters and the protective gas for the material deposition by robotic welding on a steel plate.
  2. Programming of the robot's trajectories.
  3. Experimental aquisition of the temperatures based on two non-contact measurement systems.
  4. 3D scanning of the welded specimen and reconstruction of the surfaces by reverse engineering techniques.
  5. Variation of the gas flow rate for several sets of plates.
  6. Synchronization of the times from the temperature acquisition procedures (pyrometer and thermography camera) with the robot's working program.

7. Performing a visual inspection doubled by measurements of the specimens obtained by robotic material deposition for: determination of the number of droplets, determination of the slag crust, geometric irregularities, marginal craters, solid film deposits, weld bead width, weld bead height.
8. Use of cutting and grinding machines for sampling and polishing the surfaces of the specimens.
9. Preparation of the surfaces of the specimens by applying a 2% Nital based chemical reagent.
10. Analysis of the specimens with an optical microscope and processing of the results with the help of a specialized program.

- **Methodological** contributions:
    1. Use of experimental values to define the simulation conditions and to verify the results of the FEA thermal analysis.
    2. Correlation of the CFD – FEM simulation environments to capture the interaction between the fluid and solid environments.
    3. Parameterization of the geometric model by scaling the cross-sections of the bead.
    4. Implementation in MATLAB environment of the Nishikawa methodology for identifying the constants of the first-order systems.
    5. Synchronization of the values of the conductance and capacitance corrections anticipated by the regression algorithm with the transient thermal analysis model.
    6. Correlation of the geometric parameters, microstructural defects and dilution with the dynamic system correction coefficients by multiple linear regression

- **Modeling-simulation** contributions:
    1. Development of a CFD simulation model for evaluating the forced convection coefficient produced by the protective gas flow.
    2. Development of a FEM simulation model for evaluating the temperature distribution in robotic material deposition.
    3. Sensitivity study of the simulation model to the variation of conductance and capacitance.
    4. Improvement of the simulation model by introducing experimental data

6.3 Future work

Based on the state of art study of the Doctoral Thesis, as well as the conclusions and observations during the research, the following research topics were framed:

1. Expansion of the experimental research for more steel types, including different thicknesses of the base material.
2. Using different mixtures of the protective gas to extend the model generalization.
3. Processing the data on the flow regime of the protective gas based on the recordings aquired with the high-speed camera.
4. Studying the active cooling between two consecutive passes and the consequences on the material properties.
5. Study of the influence of gas flow on additive manufacturing by electric arc welding applying Artificial Intelligence algorithms.

Selective bibliography

[1]Chen, S., Zhou, C., Tarn, T. (2007). Robotic Welding, Intelligence and Automation. Germania: Springer.

[2] Hong, T. S., Ghobakhloo, M., & Khaksar, W. (2014). Robotic welding technology. *Comprehensive materials processing*, *6*(February), 77-99.

[3] Nicolescu, A. F., Dobrescu, T. G., Ivan, M., Avram, C. G., Brad, S., Doroftei, I., & Grigorescu, S. *Roboti Industriali, Tehnologii si Sisteme de Productie Robotizate, Ed Academiei Oamenilor de Stiinta din Romania, 2011*. ISBN 978–606–8371–48–1.

[4] Alexandru, T. G., **Verdete**, **B. M**., Pupăză, C., & Nicolescu, A. F. (2019). New FEM approach including technological patterns for automotive spot welding parts. *Proceedings in Manufacturing Systems*, *14*(4), 163-168.

[5] Alexandru, T. G., & **Verdete**, **B. M.,** (2020). Knowledge-based engineering approach for facilitating weld design with the support of machine learning. 36th IBIMA international Conference, 36, 1-6.

[172] Burca, M., Negoiţescu, S. – *Sudarea MIG/MAG*, Editura Sudura(2004), ISBN 973-8359-22-8, Timişoara.

[174] **Verdete**, **B. M**., Rontescu, C., & Alexandru, T.G. (2022). Capturing the temperature gradients of GMAW hardfacing processes by employing CFD and FEM simulation procedures. In MATEC Web of Conferences (Vol. 373). EDP Sciences, 65-77.

[181] Kuijper, M. (2012). First-order Representations of Linear Systems. Germania: Birkhäuser Boston.

[182] Bi, Q., Cai, W. J., Lee, E. L., Wang, Q. G., Hang, C. C., & Zhang, Y. (1999). Robust identification of first-order plus dead-time model from step response. *Control Engineering Practice*, *7*(1), 71-77.

[183] Kumar, A., Rana, S., Gori, Y., & Sharma, N. K. (2021). Thermal Contact Conductance Prediction Using FEM-Based Computational Techniques. In *Advanced Computational Methods in Mechanical and Materials Engineering* (pp. 183-217). CRC Press.

[184] **Verdete**, **B. M**., Pupăză, C., & Alexandru, T. G. (2023). Reduced order model for evaluating the temperature gradients of the surfacing weld process. *Romanian Journal of Information Technology and Automatic Control*, *33*(1), 7-20.

[185] Nishikawa, H. (2007). A first-order system approach for diffusion equation. I: Second-order residual-distribution schemes. *Journal of Computational Physics*, *227*(1), 315-352.

[186] Stoicuta, O., & Mandrescu, C. (2012), Identificarea sistemelor, România: Editura Universitas din Petroşani

[187] Riabcev, I. A., Rosert, R., Senczenkov, I. K., & Turyk, E. (2017). Welding Imperfections in Surfaced Layers. *Biuletyn Instytutu Spawalnictwa*, *61*(3), 17-28.

[188] ***, Standard SR-EN 5817:2003.